

ARTICLE

Received 5 Jan 2012 | Accepted 11 Apr 2012 | Published 22 May 2012

DOI: 10.1038/ncomms1838

# Microtubule and cortical forces determine platelet size during vascular platelet production

Jonathan N Thon<sup>1,2</sup>, Hannah Macleod<sup>1</sup>, Antonija Jurak Begonja<sup>2,3</sup>, Jie Zhu<sup>4</sup>, Kun-Chun Lee<sup>4</sup>, Alex Mogilner<sup>4</sup>, John H. Hartwig<sup>2,3</sup> & Joseph E. Italiano Jr<sup>1,2,5</sup>

Megakaryocytes release large preplatelet intermediates into the sinusoidal blood vessels. Preplatelets convert into barbell-shaped proplatelets *in vitro* to undergo repeated abscissions that yield circulating platelets. These observations predict the presence of circular-preplatelets and barbell-proplatelets in blood, and two fundamental questions in platelet biology are what are the forces that determine barbell-proplatelet formation, and how is the final platelet size established. Here we provide insights into the terminal mechanisms of platelet production. We quantify circular-preplatelets and barbell-proplatelets in human blood in high-resolution fluorescence images, using a laser scanning cytometry assay. We demonstrate that force constraints resulting from cortical microtubule band diameter and thickness determine barbell-proplatelet formation. Finally, we provide a mathematical model for the preplatelet to barbell conversion. We conclude that platelet size is limited by microtubule bundling, elastic bending, and actin-myosin-spectrin cortex forces.

<sup>1</sup> Hematology Division, Department of Medicine, Brigham and Women's Hospital, Boston, Massachusetts 02115, USA. <sup>2</sup> Harvard Medical School, Boston, Massachusetts 02115, USA. <sup>3</sup> Translational Medicine Division, Brigham and Women's Hospital, Boston, Massachusetts 02115, USA. <sup>4</sup> Department of Neurobiology, Physiology and Behavior and Department of Mathematics, University of California Davis, Davis, 95616, USA. <sup>5</sup> Vascular Biology Program, Department of Surgery, Children's Hospital, Boston, Massachusetts 02115, USA. Correspondence and requests for materials should be addressed to J.E.I. (email: jitaliano@rics.bwh.harvard.edu).

Human adults have ~1 trillion circulating blood platelets (PLTs), and, because the lifespan of an individual PLT is only 8–10 days, 100 billion new PLTs are produced daily from bone marrow megakaryocytes (MKs) to maintain their  $150\text{--}400 \times 10^9 \text{ l}^{-1}$  counts in whole blood. PLTs are anucleate discoid cells 1.5–3  $\mu\text{m}$  in diameter. Among their primary functions, PLTs serve as the ‘band-aids’ of the bloodstream and respond to blood vessel injury by changing shape, secreting their granule contents, and aggregating to form a PLT clot. These responses, while advantageous for haemostasis, can become undesirable, if they cause tissue ischemia or infarction. Despite a growing list of PLT-associated disorders, resulting from higher-than-normal or lower-than-normal PLT counts<sup>1</sup>, the terminal stages of PLT production and ultimate determinants of PLT size remain unknown.

The current model of PLT formation recognizes that, on reaching maturity, bone marrow MKs will extend, through junctions in the lining of blood sinuses, long, branching proPLTs. These dynamic intermediate structures are consisted of tandem arrays of slender tubular projections cored by microtubule bundles with PLT-sized swellings at their ends. ProPLT-producing MKs in culture release intermediate barbell structures that yield individual PLTs<sup>2,3</sup>. ProPLTs have been identified extending and releasing into blood vessel sinusoids both *in vitro* and *in vivo*<sup>4,5</sup>, and are therefore believed to mature in the circulation<sup>3,6</sup>. We have recently identified a new intermediate stage called the prePLT in the maturation process. PrePLTs are anucleate discs 3–10  $\mu\text{m}$  across that reversibly convert into barbell-shaped proPLTs to divide and form two PLTs<sup>7</sup>.

Here we show that circular-prePLTs and barbell-proPLTs are present in human whole blood, and quantify them using a laser scanning cytometry assay. We propose and test a biological model for terminal PLT production that predicts marginal microtubule coil diameter and thickness determine barbell-proPLT formation and regulate PLT size. Lastly, we provide a mathematical and computational model that is based on the balance of microtubule bundling forces, elastic bending forces, and actin-spectrin-myosin cortex forces to describe the mechanism of circular-prePLT to barbell-proPLT conversion.

## Results

**Identification of the critical prePLT size.** To establish the morphometric characteristics of circular-prePLTs and barbell-proPLTs that will be used to quantify them in whole blood, we employed a quantitative immunofluorescence microscopy-based assay. Released proPLT cultures were isolated as previously described<sup>7</sup>, spun down onto poly-L-lysine-coated glass coverslips, and probed for the MK lineage-specific  $\beta 1$ -tubulin isoform to delineate the cell periphery. Five-by-five composite images were generated from individual images taken at  $\times 20$  magnification and collected for at least 3 different samples (Fig. 1a). Individual cells were thresholded based on a binary image mask and analysed across multiple morphometric parameters including area, circularity, perimeter and number.

Quantitative immunofluorescence microscopy of released proPLT cultures was validated using human and mouse PLT controls (Fig. 1b). To distinguish intermediates in PLT production, objects identified by quantitative immunofluorescence microscopy in murine proPLT cultures were categorized as resting PLTs, circular-prePLTs, or barbell-proPLTs based on their circularity and perimeter measurements (Fig. 1c). Precise measurements of mouse proPLT culture intermediates revealed a minimum perimeter for barbell-proPLTs of ~10  $\mu\text{m}$  (Fig. 1d), which translates to a circular diameter of ~3  $\mu\text{m}$ . This size limit, below which barbell-proPLTs are rarely detected, was defined as the critical prePLT size, and represents the tipping point for competing forces that govern twisting of the resting PLT's marginal microtubule coil about its midsection to form the barbell-proPLT structure. An ~3- $\mu\text{m}$  diameter threshold

was therefore established to distinguish discoid PLTs, which are incapable of undergoing barbell-proPLT conversion, from their circular-prePLT progenitors. Examination of human PLT-rich plasma (PRP) using this approach predicted the presence of circular-prePLTs and barbell-proPLTs in whole blood (Fig. 1e), which adhered to the size constraints governing circular-prePLT to barbell-proPLT conversion established in murine cell cultures (Fig. 1f).

Large PLTs often occur concomitantly with periods of PLT depletion in humans<sup>8</sup> and various forms of MK processes, and proPLTs are present in cytospin preparations of human PRP<sup>9</sup>. Nevertheless, because barbell-proPLTs are not detected in human blood smears, it is unclear whether these circulate in blood, and their role in thrombocytopenia has not been studied. To demonstrate the existence of circular-prePLTs and barbell-proPLTs in the circulation, and establish the experimental conditions for their detection and subsequent quantification, whole blood from the same human donor was collected into 10% AJ buffer or sodium citrate, EDTA, and heparin tubes (anticoagulant) ( $n=3$ ). Representative Giemsa-stained blood smears in Fig. 2a demonstrate the presence of barbell-proPLTs and circular-prePLTs in AJ buffer and sodium citrate, but not in EDTA- and heparin-treated blood. EDTA has been shown to affect proPLT concentration in the venous and arterial circulation of rats and cause PLT spherizing<sup>10</sup>. Immunofluorescence microscopy images of  $\beta 1$ -tubulin-stained PRP from EDTA- and Heparin-treated blood confirmed this, and revealed smaller PLTs with thicker/brighter microtubule coils (Fig. 2b). These results account for why barbell-proPLTs have not previously been reported in human blood smears and establish important experimental preconditions for quantification of PLT production intermediates from whole blood.

**Quantification of PLT intermediates in blood.** To overcome the quantification limitations of immunofluorescence microscopy, and more accurately identify specific intermediate forms in PLT production from whole blood, we developed a laser scanning cytometry assay. Human PRP was isolated and probed for  $\beta 1$ -tubulin on poly-L-lysine-coated glass coverslips. Supplementary Fig. S1a illustrates the laser scanning cytometry analysis work flow for the detection and quantification of intermediates in PLT production from PRP. Resting PLTs, circular-prePLTs, and barbell-proPLTs were differentially gated based on morphological and signal-level dependent scattergram analysis from which a representative image gallery was generated (Fig. 3a). Barbell-proPLTs in human whole blood were distinguished from circular/discoid objects based on their unique barbell morphology, and ranged in perimeter from roughly 10–32  $\mu\text{m}$  (or 3–10  $\mu\text{m}$  in diameter if assumed to convert into circular objects). These observations support previous measurements of barbell-proPLTs and circular-prePLTs in cell culture presented in Fig. 1. Circular-prePLTs in human whole blood were therefore distinguished from discoid PLTs based on their ability to convert into barbell shapes<sup>7</sup>, and gated based on the empirically determined diameter of ~3  $\mu\text{m}$ . This enabled us to determine circular-prePLT and barbell-proPLT counts in whole blood, which comprised 3.63 and 0.05% of PLT counts, respectively (Fig. 3b).

**Biological model of proPLT conversion.** The demonstration that prePLTs can undergo barbell-proPLT conversion while PLTs cannot, led us to propose the following biological model of vascular PLT production: Force constraints resulting from cortical MT band diameter and thickness determine barbell formation and account for circulating discoid PLT size. This model makes three fundamental biological predictions regarding the mechanism of proPLT conversion. If peripheral microtubule coil thickness is kept constant, large PLTs will undergo barbell-proPLT conversion whereas small PLTs will not. Thinner peripheral microtubule coils will be more able to overcome resistance to elastic bending forces that limit

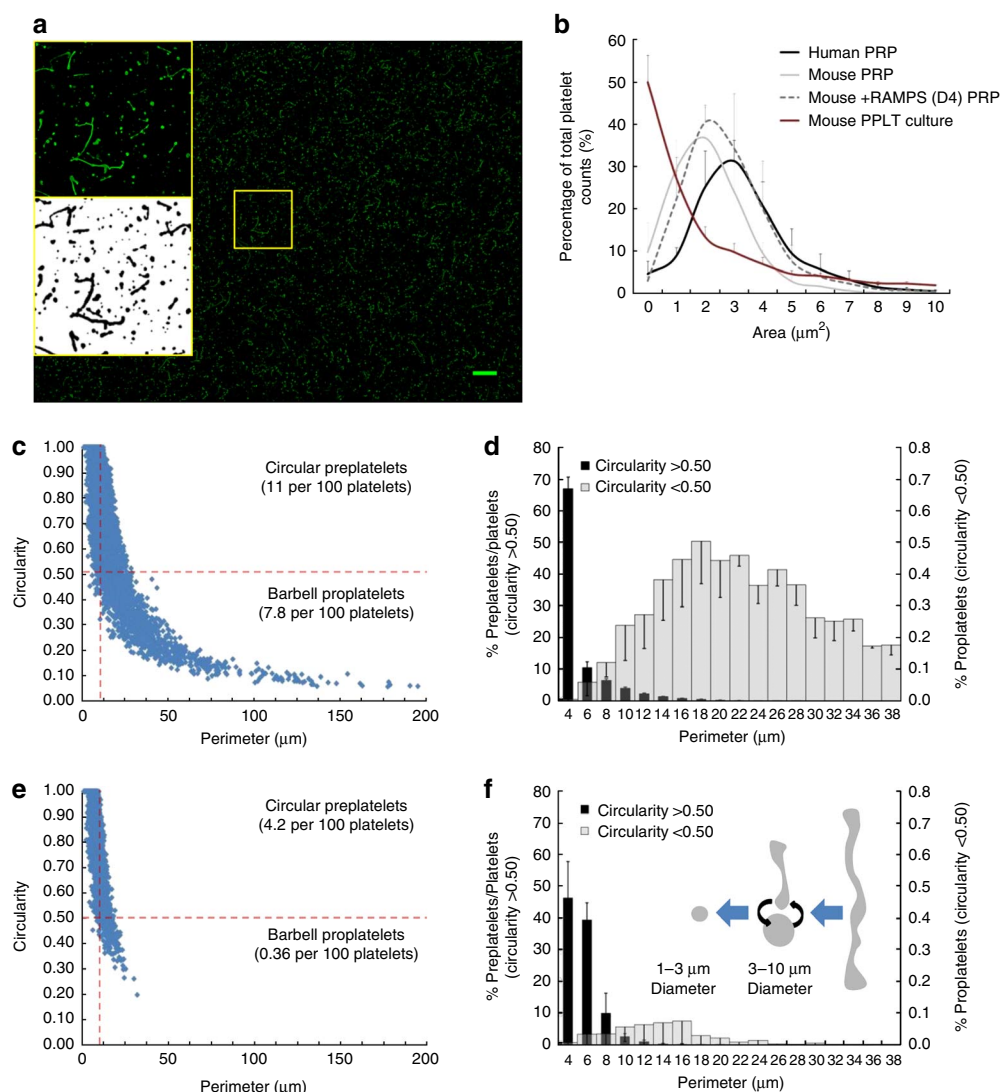


**Figure 1 | Quantitative immunofluorescence microscopy of mouse and human proPLTs.** (a) Composite image of mouse FLC proPLTs. Objects were identified by their fluorescence intensity, and thresholded on a binary mask to quantify area, circularity, perimeter, and number. (b) Validation of approach using mouse/human PLT controls. (c) Circularity/perimeter measurements from mouse FLC cultures. (d) A minimum perimeter for barbell-proPLTs and maximum diameter for circular-prePLTs of  $\sim 10 \mu\text{m}$  was used to establish a  $\sim 3 \mu\text{m}$  diameter threshold to distinguish circular-prePLTs from PLTs in mouse FLC cultures. (e) Human PRP reveal PLT-intermediates in whole blood. (f) Human PRP. Analyses were performed for at least three independent samples. Error bars represent 1 s.d. about the mean. Scale bar,  $50 \mu\text{m}$ .

barbell-proPLT conversion than thicker microtubule coils. The elongating microtubule bundle is deformed by the external compressive pressure of the actin-myosin-spectrin cortex.

ProPLT elongation by bone marrow MKs, and circular-prePLT to barbell-proPLT conversion are primarily driven by reorganization of the microtubule cytoskeleton. The development of an *in vitro* assay to separate circulating human PLT intermediates from red blood cells (RBCs) (Supplementary Methods) enabled us to finely assess vascular proPLT/prePLT ultrastructure by thin section and negative stain electron microscopy. Whole blood-derived prePLT/proPLTs were cytoplasmically indistinguishable from mature PLTs and large PLT-like intermediates from mouse MK cell cultures (Fig. 4a,b) and contained comparable numbers of peripheral microtubules (Fig. 4c,d; Supplementary Fig. S2). PLTs from Filamin A knock-out (KO) mice were included as a positive control because they are known to be larger than normal circulating mouse PLTs and contain thicker microtubule coils<sup>11</sup>. These data establish the experimental preconditions by which to test biological prediction 1.

Biological prediction 1 stipulates that above a threshold diameter elongating microtubules in the PLT marginal band are capable of overcoming bending energies needed to undergo barbell-proPLT conversion, whereas, below this threshold diameter, PLTs remain discoid. To increase PLT diameter, human/murine PRP was cultured at  $37^\circ\text{C}$  with gentle rotation in a humidified incubator for 0 and 6 h<sup>12</sup>, and analysed by LSC. Figure 5a shows a representative density scattergram of these cultures over time, and confirms microtubule coil enlargement at  $37^\circ\text{C}$  versus  $22^\circ\text{C}$  control (Supplementary Fig. S3a). Increased mean PLT diameter ( $\mu\text{m}$ ) for human and mouse PRP cultures are illustrated in Fig. 5b and explains lower-resting PLT and increased circular-prePLT counts, described in Fig. 5c. Increasing microtubule coil diameter resulted in more barbell-proPLT conversion relative to  $22^\circ\text{C}$  controls (Supplementary Fig. S3b), and supports our biological prediction. Samples were normalized for total object counts to address differences in PLT numbers between human replicates. These observations agree with earlier findings by Schwertz *et al.*<sup>12</sup>, and may partly account for why increases in PLT

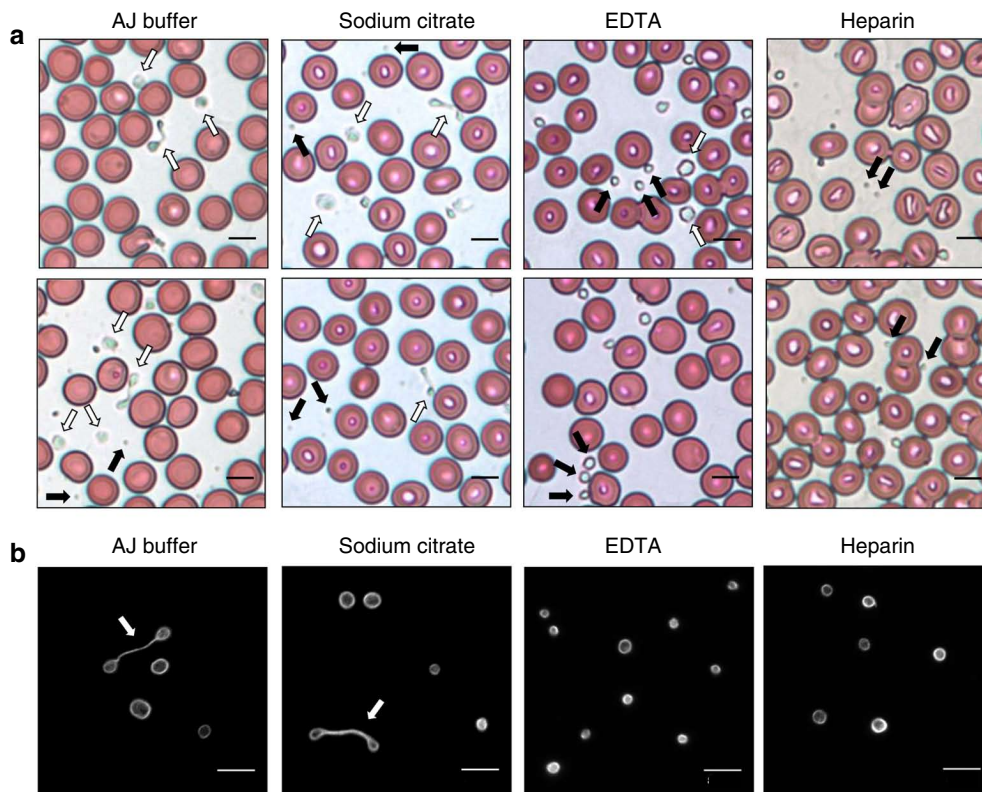


**Figure 2 | Giemsa-stained blood smears from anticoagulant-treated human whole blood. (a)** PLT intermediates were present in AJ buffer and sodium citrate, and absent in EDTA and heparin anticoagulant-treated blood smears. EDTA-treated PLTs are spherized. **(b)** Immunofluorescence images of  $\beta$ 1-tubulin-stained PRP. EDTA-treated PLTs were smaller, with more constricted microtubule coils. PLTs are indicated by black arrows, whereas circular-prePLTs or barbell-proPLTs are indicated by white arrows. Scale bar, 5  $\mu$ m.

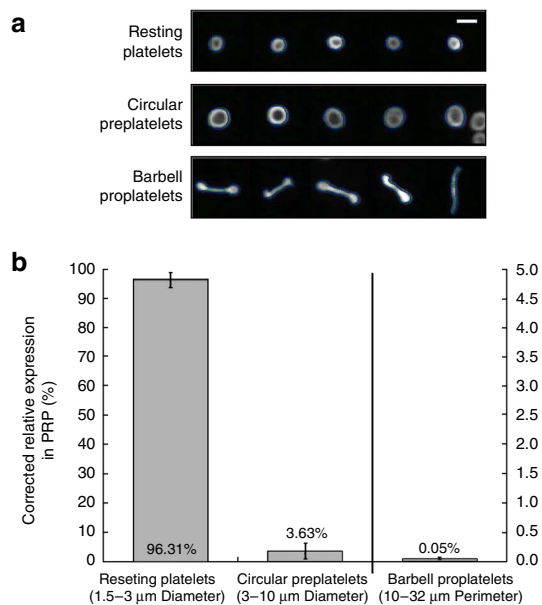


**Figure 3 | Quantification of PLT intermediates in human venous blood. (a)** Image gallery of resting PLTs, circular-prePLTs, and barbell-proPLTs differentially gated based on morphological and signal-level dependent scattergram analysis. **(b)** Resting PLT, circular-prePLT and barbell-proPLT counts from human PRP normalized for total object counts. Analyses were performed for at least three independent samples. Error bars represent 1 s.d. about the mean. Scale bar 3  $\mu$ m.

size and barbell-proPLT number have not previously been reported in the literature for PLT units, which are typically stored at 22  $^{\circ}$ C.

As mice exhibit a greater proportion of large, young PLTs in their circulation that may be equivalent to prePLTs following antibody-induced thrombocytopenia versus untreated controls (Fig. 1b)<sup>13</sup>, we hypothesized that these should form a greater number of barbell-proPLTs in circulation and in culture. To test this hypothesis PRP was isolated from mouse whole blood 4 days before and following rabbit anti-mouse platelet serum (RAMPS) infusion, and stored at 37  $^{\circ}$ C for 0 and 6 h. Expectedly, a significantly larger number of barbell-proPLTs were present in RAMPS-treated mice versus untreated controls, both at 0 and 6 h post-collection (Fig. 5d). Representative immunofluorescence microscopy images of  $\beta$ 1-tubulin-stained PRP from these samples are outlined in Supplementary Fig. S3c. Restricting microtubule coil enlargement, by comparison, should result in fewer barbell-proPLTs in culture. To test this hypothesis human whole blood was collected directly into sodium citrate, EDTA, and heparin tubes, and either stored in the same tube for 6 h at 37  $^{\circ}$ C or transferred into a new anticoagulant-treated tube every hour to restrict PLT enlargement. Representative immunofluorescence microscopy images of  $\beta$ 1-tubulin-stained PRP from these samples are outlined in Supplementary Fig. S3d. Hourly treatment of human whole blood with EDTA or heparin blood was shown to keep PLTs at a smaller size, and inhibited barbell-proPLTs relative to the sodium citrate control. These results support our biological prediction, and demonstrate that force constraints resulting from cortical microtubule band diameter regulate barbell-proPLT formation.

If barbell-proPLT formation is determined by the balance of microtubule bundling and elastic bending forces, thinner peripheral microtubule coils will more easily undergo barbell-proPLT conversion

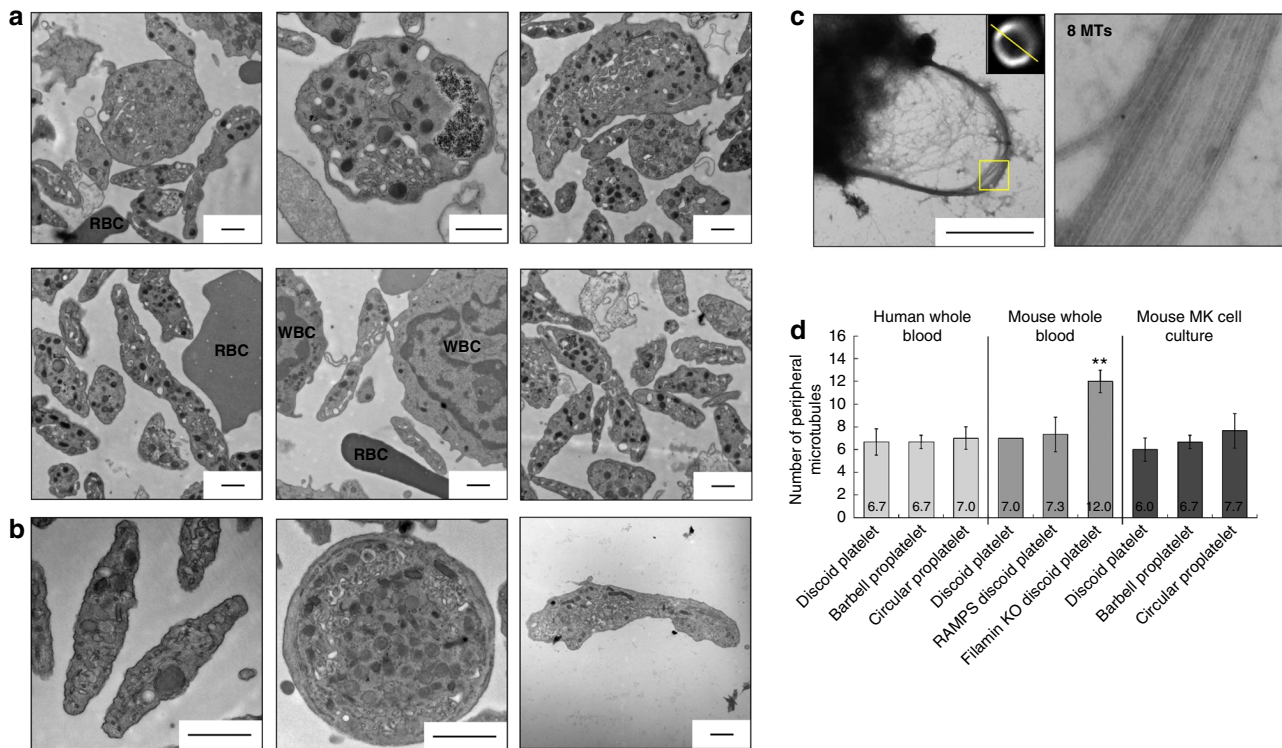


**Figure 4 | Ultrastructural analysis of PLT intermediates.** (a) Thin-section EMs of human whole-blood PLTs, circular-prePLTs (top), and barbell-proPLTs (bottom). (b) EMs of mouse blood PLTs (left), FLC circular-prePLT (middle) and FLC barbell-proPLT (right). (c) Negative-stained EM and immunofluorescence micrograph with linescan (insert) of human whole-blood PLT used to measure the number, size and fluorescence intensity of the peripheral microtubule band. (d) Quantification of negative-stained EMs revealed 6–8 peripheral microtubules in PLTs, barbell-proPLTs and circular-prePLTs. PLTs from Filamin A KO mice shown as a positive control. Analyses were performed for at least three independent samples. Error bars represent one standard deviation about the mean. Statistical significance was established using a one-tailed Student's *t*-test for paired samples (\*\* $P < 0.01$ ). Scale bar, 1  $\mu\text{m}$ .

than thicker ones. To inhibit microtubule polymerization, PLTs were incubated with increasing concentrations of nocodazole, and cultured at 37°C for 6 h. Nocodazole-treated PLTs did not become larger (Fig. 5f), and resulted in increased numbers of smaller barbell-proPLTs relative to the DMSO control (Fig. 5d and e), which agree with our predictions. Alternatively, we looked at filamin A KO mouse PLTs, which are significantly larger than their wild-type (WT) controls (Fig. 5f)<sup>11</sup>, contain thicker microtubule coils (Fig. 4d), and were shown to increase proportionately in size, following incubation at 37°C for 6 h (Fig. 5f). Barbell-proPLTs in these samples were present at a concentration of ~40% that of WT controls, were larger, and formed irregular shapes in culture (Fig. 5g). These results demonstrate that microtubule bundling forces and elastic bending forces determine critical prePLT size.

For peripheral microtubule coil lengthening to buckle, driving proPLT formation, the expansion force that is generated by microtubule coil sliding and/or polymerization must be checked by an equally strong compressive force deriving from the cell cortex. To test this prediction, proPLTs were treated with the actin-destabilizing drugs latrunculin and cytochalasin D for 2 h, which were shown to increase proPLT end size, and the actin-stabilizing drug jasplankinolate, which was shown to decrease proPLT end size, relative to the DMSO control (Fig. 5h). We have also recently shown that barbell proPLTs treated with the spectrin disrupting peptide  $\text{sp}\alpha 2\text{N}1$  are unable to retain their barbell shape and collapse into a circular prePLT form<sup>14</sup>. These observations confirm that elongating microtubule bundles in the peripheral coil are being deformed by the external compressive pressure of the actin-myosin-spectrin cortex during proPLT conversion.

**Mathematical model of proPLT conversion.** As barbell-proPLT conversion is regulated by microtubule coil diameter and thickness, we hypothesized that the balance between the elastic bending forces of the peripheral microtubule bundle and the effective actin-spectrin-myosin cortex tension determine barbell-proPLT shape and critical prePLT size (Fig. 6a). To test this hypothesis, we developed a mathematical model of circular-prePLT deformation during which the perimeter of the peripheral microtubule bundle was increased while cell area was maintained constant by a rigid actin-myosin-spectrin cortex (Fig. 6b; Supplementary Movie 1). As the microtubule bundle elongated, the middle part of the cell narrowed, until the opposite parts of the microtubule bundle touched, forming a barbell-proPLT structure. On reaching this point, microtubule associated proteins crosslink the microtubule bundle creating a 'corridor' between the lobes of the barbell-shaped cell. *In vivo*, the peripheral microtubule coil twists about its midsection to form the barbell-proPLT structure<sup>7</sup>. To validate that our model was accurately representing this, the energy of a twisted microtubule bundle of two microtubules as a function of the helical pitch was modelled, and the energy minimum it described corresponded to the predicted pitch of the twisted microtubule bundle (Supplementary Fig. S4). These results demonstrate that twisting of the microtubule bundle in the barbell-proPLT shaft can lower the sum of the bundling elastic energies to account for this process *in vivo*.

This computational model makes a number of biological predictions that are supported by our data (Supplementary Methods). First, calculations show that the effective force needed to expand and bend the peripheral microtubule bundle during circular prePLT to barbell-proPLT conversion is inversely proportional to

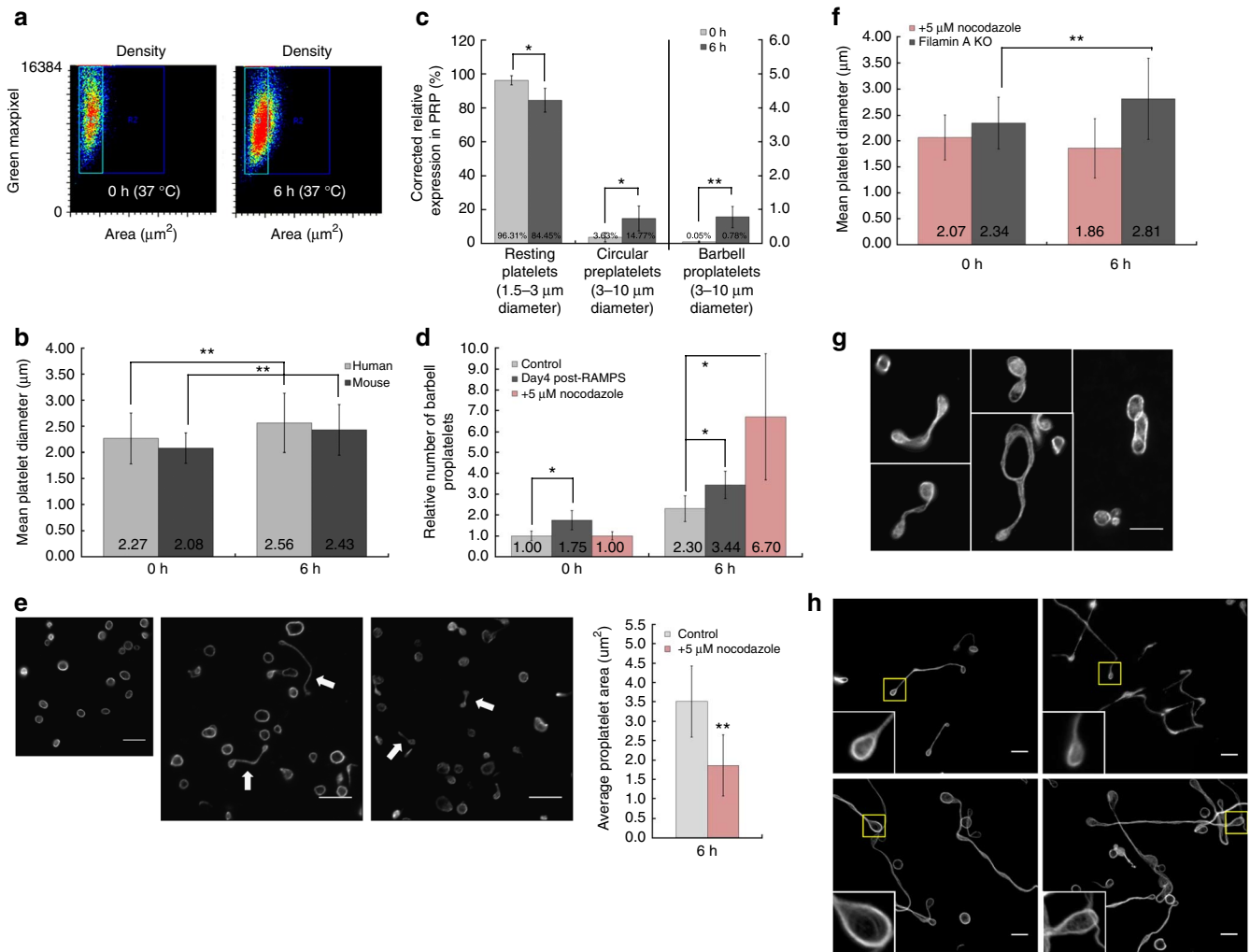


**Figure 5 | Structural determinants of proPLT conversion.** (a) Density scattergrams of human PRP. PLTs and circular-prePLTs are represented by a cyan and blue box, respectively. (b) Mean diameter of resting PLTs increased following incubation at 37 °C. (c) Increasing PLT size resulted in lower relative PLT counts, higher circular-prePLT counts and increased barbell-proPLT conversion in human PRP at 37 °C. (d) Mouse PRP at 37 °C. Larger PLTs from RAMPS-treated mice produced more barbell-proPLTs than WT controls. (e) Relative to DMSO 0 h. (left) and 6 h. (middle) controls, 5 μM nocodazole treatment (right) generated increased numbers of smaller barbell-proPLTs (white arrows). (f) Mean diameter of nocodazole-treated and filamin KO mouse PLTs following incubation at 37 °C. (g) PRP from filamin A KO mice demonstrate larger, irregular shaped proPLTs at concentrations ~40% of WT controls. (h) Relative to DMSO control (top-left), actin-stabilizing drug jasplankinolide (top-right), and destabilizing drugs latrunculin (bottom-left) and cytochalasin D (bottom-right) decreased/increased proPLT end size, respectively. Analyses were performed for at least three independent samples. Error bars represent 1 s.d. about the mean. Statistical significance was established using a one-tailed Student's *t*-test for paired samples (\* *P* < 0.05, \*\* *P* < 0.01). Scale bar, 5 μm.

prePLT area:  $f \propto L_0^{-2}$  (Supplementary Fig. S4). Assuming that this force is generated by microtubule motors (for example, cytoplasmic dynein) and microtubule polymerization, and does not scale with circular-prePLT size (or changes relatively slowly with the size), our model predicts that, below a certain size threshold, this force will be insufficient to elongate the microtubule bundle. In other words, while microtubule number and diameter regulate PLT size, pre-PLT intermediates are not required to have thicker peripheral microtubules. Increasing the number of peripheral microtubules, however, will result in terminal platelets of a larger proportional size owing to their inability to undergo further barbell-proplatelet conversion. Indeed, Figs 1d and 6c confirm this hypothesis for our proPLT cultures and indicate that the respective critical prePLT diameter in these samples is  $\sim 10 \mu\text{m}$ . This is not an absolute threshold, and critical prePLT size is predicted to depend on the number of microtubule motors and peripheral microtubules in the cell. Second, these data indicate that when circular-prePLT size is greater than critical,

the perimeter of the resulting proPLT scales as  $L \propto L_0^{-2}$  (Fig. 6c). This model lets us explain this scaling in one of three ways: total amount of tubulin scales with prePLT area; proPLTs stop deforming when the motor force density that scales as  $f_{\text{mot}} \propto L_0^{-1}$  (constant number of motors distributed over distance  $L$ ) decreases to the necessary microtubule tensile force  $f \propto L_0^{-2}$  cell area remains constant throughout PLT morphogenesis. Third, final PLT size can be explained by this model as resulting from the balance between the bundling force and microtubule elastic bending force. When characteristic protein forces and microtubule rigidity are factored in, the predicted PLT radius is calculated to be in the micron range, as observed. Fourth, this model predicts that PLT size increases slowly as the microtubule number in the peripheral bundle cross-section grows. This agrees with measurements of WT and filamin A KO PLTs that show, when the microtubule number increases from 7 to 12 (Fig. 4d), baseline PLT size increases from 2.08 (Fig. 5b) to 2.34 μm (Fig. 5f). During cell culture at 37 °C, PLT diameters are increased,

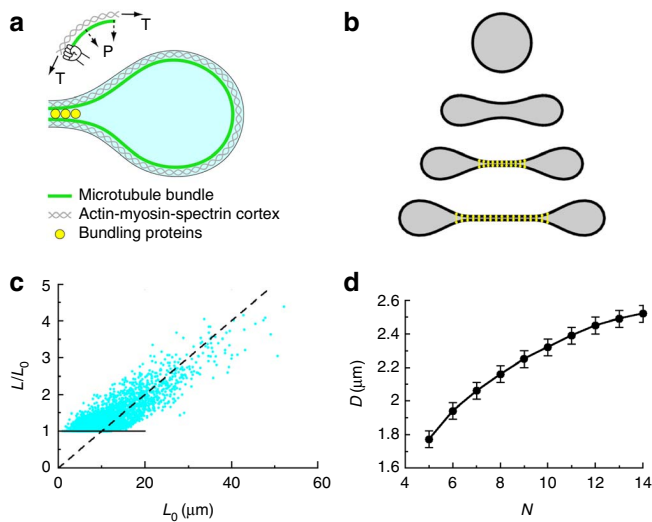


**Figure 6 | Mathematical modelling of barbell-proPLT conversion.**

(a) Schematic of force balance as outlined by Laplace's Law ( $P$  = pressure,  $T$  = cortex tension). (b) Simulated shapes in proPLT conversion. After corridor formation, microtubule-bundling proteins (short yellow lines) 'zip up' the corridor. From top to bottom, the ratio of shown cell perimeter to initial, circular, perimeter:  $L/L_0 = 1, 1.5, 2, 2.5$ . (c) Circularity relation.  $L_0$  = perimeter of the initial circular-prePLT,  $L$  = perimeter of the barbell-proPLT. Solid line:  $L/L_0 = 1$ . Dashed line:  $L/L_0 = L_0/(10\mu\text{m})$ . (d) Simulated PLT diameter vs number of microtubules in the bundle. Analyses were performed for at least three independent samples. Error bars represent 1 s.d. about the mean.

possibly driven by microtubule sliding and/or polymerization, resulting in barbell-proPLT formation. Figure 6d summarizes this relationship by illustrating computed PLT size as a function of microtubule number. This model establishes the mechanism describing a terminal stage in PLT production and makes important predictions that can be tested to account for well-defined differences in mean PLT size among different mouse strains, and compared with mouse/human macrothrombocytopenias to identify important cytoskeletal interactions affecting normal PLT production.

## Discussion

We present here three new insights into the terminal mechanisms of PLT production. First, we accurately quantify circular-prePLTs and barbell-proPLTs in human blood from high-resolution fluorescence images by a laser scanning cytometry assay. This advance overcomes the quantification limitations of microscopy and qualitative limitations of flow cytometry that have previously been employed, and shifts the paradigm of PLT release from bone marrow MKs towards large PLT-like intermediates in the blood. From it, we conclude that circular-prePLTs are dynamic intermediate structures in platelet production. Given the relatively low concentration of barbell-proPLTs in venous blood, it is possible that, once circular-prePLTs convert into barbell-proPLTs, abscission is rapid. Alternatively, prePLTs may become trapped in the micro-capillaries of the bone marrow, lung and/or spleen where intravascular shear forces can drive PLT production. Indeed, reports of higher PLT counts in post-pulmonary vessels suggests that the lung may be a milieu for terminal PLT formation<sup>15</sup>. Second, we show that twisting microtubule-based forces driving circular-prePLT to barbell-proPLT conversion are governed by two major biophysical properties: microtubule coil diameter and microtubule coil thickness. Indeed, large PLTs from patients with Gray PLT syndrome, May-Hegglin anomaly, and Epstein's syndrome contain 10–20-fold increased numbers of peripheral microtubule

coils relative to normal human PLTs, which agree with our predictions<sup>16</sup>. Many giant PLTs also contain peripheral microtubules, organized like balls of yarn, that may explain why the majority of these cells have a spherical rather than discoid form<sup>16</sup>. Last, these observations have allowed us to address what forces determine barbell-proPLT formation and establish a mechanism for how the final PLT size is established. Barbell-proPLT conversion is an elaborate and complex process that defines the morphology and ultrastructure of circulating PLTs. PLT number and size are often inversely proportional, and others have shown that the PLT cytoskeleton can regulate PLT size and numbers through specific transmembrane receptor interactions. GPIb, for example, is complexed to the actin-binding protein filamin A and is known to have an important role in maintaining the normal cytoskeletal architecture of resting PLTs<sup>17,18</sup>. In Bernard Soulier Syndrome genetic abnormalities of the GPIb-IX-V complex, particularly the GPIb $\alpha$  subunit that contains the Von Willebrand factor and thrombin-binding sites, results in fewer and larger PLTs<sup>1</sup>. As normal numbers of MKs are generally found in the bone marrow of these patients, it is likely that the macrothrombocytopenia is related to an error in the terminal stages of PLT production. Moreover, the novel identification of an autosomal dominant macrothrombocytopenia associated with PLT dysfunction in Glanzmann's Thrombasthenia<sup>19</sup> raises interesting questions about the role of GPIIb/IIIa and its beta terminal domain in proPLT formation and PLT release. Myosin IIA, the non-muscle myosin heavy chain product of the *MYH9* gene, has also been implicated in restraining proPLT formation in developing MKs<sup>20</sup>. In the case of *MYH9*-RD, defective myosin IIA could promote premature proPLT formation in the osteoblastic niche through loss of attenuation, or result in defective proPLT formation and reduced or abnormal PLT release in the vasculature<sup>21</sup>. Indeed, patients with autosomal dominant inherited *MYH9*-RDs (for example, May-Hegglin anomaly) generally exhibit macrothrombocytopenia as well as variable degrees of hearing loss, nephritis and cataracts<sup>21</sup>. Here we provide a mathematical model of circular-prePLT to barbell-proPLT conversion that is based on the balance of microtubule bundling forces, elastic bending forces, and actin-spectrin-myosin cortex forces. Biophysical modelling of the cytoskeletal forces driving barbell-proPLT conversion provide insight into PLT size determination that will be used to study human macrothrombocytopenias. A better understanding of the cytoskeletal mechanisms that regulate PLT formation will lead to the development of improved therapies for clinical disorders of PLT production and an important source of PLTs for infusion.

## Methods

**Megakaryocyte suspension cultures.** Mouse FLCs were collected from WT CD1 mice (Charles River Laboratories, Wilmington, MA) on day E13.5, and cultured at 37°C and 5% CO<sub>2</sub> in the presence of 0.1  $\mu\text{g ml}^{-1}$  purified recombinant mouse c-Mpl ligand for 5 days. Round MKs, proPLT-MKs and released proPLTs were isolated by BSA gradient sedimentation, and cultured separately as previously described<sup>7</sup>. All studies complied with institutional guidelines approved by the Boston Children's Hospital animal care and use committee, and the IACUC.

**Human/murine whole-blood PLTs.** Human blood was obtained by venipuncture from healthy volunteers, as previously described<sup>22</sup>, and collected into 0.1-volume AJ buffer (85 mM sodium citrate, 69 mM citric acid, 20 mg ml<sup>-1</sup> glucose) or Sodium Citrate (blue-capped), EDTA (purple-capped), and Heparin (green-capped) anticoagulant tubes. Collections were performed in accordance with ethics regulation with IRB approval, and informed consent was provided according to the Declaration of Helsinki. Murine blood was obtained by retro-orbital bleed into 0.1-volume AJ anticoagulant from anaesthetized CD1 strain mice, as previously described<sup>23</sup>. For RAMPS-treated mice, CD1 strain mice were injected with 50  $\mu\text{l}$  RAMPS (Inter-cell technologies, Jupiter, FL) intraperitoneally to induce thrombocytopenia. Whole blood was collected on Day 4 post-injection, as PLT counts were recovering, and again 2 weeks later (normal control). Samples were centrifuged at 1,000g for 5 min to isolate PRP, and stored at 37°C and 5% CO<sub>2</sub> with gentle rotation for 0 or 6 h.

**Immunofluorescence microscopy.** Megakaryocytes, proPLT-MKs, released proPLTs, and whole-blood PLTs were purified and probed, as previously described<sup>24</sup>.

Briefly, samples were fixed in 4% formaldehyde and centrifuged onto poly-L-lysine ( $1 \mu\text{g ml}^{-1}$ )-coated coverslides (resting), or spun directly onto poly-L-lysine-coated coverslides and allowed to spread for 20 min at room temperature before fixation (spread). For analysis of cytoskeletal components, samples were permeabilized with 0.5% Triton-X-100, and blocked in immunofluorescence blocking buffer (0.5 g BSA, 0.25 ml 10% sodium azide, 5 ml FCS, in 50 ml  $1\times$ PBS) overnight before antibody labelling<sup>25</sup>. To delineate the microtubule cytoskeleton, samples were incubated with a rabbit polyclonal primary antibody for human  $\beta$ 1-tubulin generated against the carboxy-terminal peptide sequence CKAVLEEDVEETEEAEMEPED-KGH (Genemed Synthesis, San Antonio, TX), washed, and probed with a secondary Alexa 488 nm-conjugated goat anti-rabbit antibody (Invitrogen).

For examination of PLT surface receptor expression in non-permeabilized cells, samples were kept resting, fixed and centrifuged onto poly-L-lysine-coated coverslides as described without the 0.5% Triton-X-100 incubation, and probed with fluorescein isothiocyanate (FITC)-conjugated antibodies against GPIIIa (Beckton Dickinson). To correct for background fluorescence and nonspecific antibody labelling, slides were incubated with the secondary antibody alone or a PE-conjugated IgG antibody control, and all images were adjusted accordingly. Samples were examined with a Zeiss Axiovert 200 (Carl Zeiss, Thornwood, NY) equipped with a  $\times 63$  (NA = 1.4) Plan-ApoChromat oil immersion objective, and images were obtained using a Hamamatsu charged coupled device camera (Bridgewater, NJ). Images were analysed using the Metamorph image analysis software (Molecular Devices, Sunnyvale, California, USA) and ImageJ (NIH, <http://rsb.info.nih.gov/ij/>).

**Blood smears.** Human whole-blood smears were generated by placing a 5–1 drop at one end of a conventional glass slide and pulling the drop along the length of the slide using a second glass slide at a 45° angle. Blood smears were fixed and Giemsa-stained using the Diff-Quick staining kit as per the manufacturer's instructions (Siemens, Washington, DC).

**Laser scanning cytometry.** Platelet-rich plasma was spun down onto poly-L-lysine-coated glass coverslides, fixed, permeabilized, and probed for  $\beta$ 1-tubulin, as previously described. Laser scanning cytometry was performed on the iCys Research Imaging Cytometer (CompuCyte, Westwood, Massachusetts, USA); a microscope-based cytofluorometer that employs wide-field laser-spot scanning illumination, and was used to detect  $\beta$ 1-tubulin localization in our samples at 488 nm (ref. 26). Briefly, coverslides were scanned at a  $\times 20$  magnification (low-resolution mosaic scan) to generate DIC and fluorescence image maps of the sample slides. Fifty '5 $\times$ 5' regions of interest were selected from these image maps to uniformly represent the entire sample preparation while avoiding air-bubbles, coverslide borders, and imperfections in the glass. Samples were then scanned using a  $\times 60$  objective (field scan) to generate fluorescence region maps composed of 25 high-resolution images. These were processed using manufacturer-developed modules to threshold individual objects based on known human PLT parameters and contour these events for subsequent quantitative analysis. Data were subject to morphological and signal-level-dependent scattergram analysis using the iCys image analysis software (CompuCyte), and barbell-proPLTs, 'figure 8' proPLTs, circular-prePLTs, resting PLTs and activated PLTs were gated based on a combination of area, perimeter, circularity, integral, fluorescence intensity, and maximum pixel intensity. For the purposes of exactness in all subsequent quantifications, figure '8' proPLTs, activated PLTs, and PLT clumps were excluded from the analysis. Analysis of barbell-proPLT, circular-prePLT, and discoid PLT numbers were performed for at least three independent samples. Error bars represent 1 s.d. about the mean. Statistical significance between 0– and 6 h time points was established using a one-tailed Student's *t*-test for paired samples ( $*P < 0.05$ ,  $**P < 0.01$ ).

**Red blood cell lysis.** Whole blood was collected as described above, and immediately fixed with 1% or 0.1% formaldehyde. Samples were transferred into 2 volume equivalents of RBC lysis buffer (150 mM  $\text{NH}_4\text{Cl}$ , 10 mM  $\text{KHCO}_3$ , 0.1 mM EDTA, pH 7.2–7.4) and incubated at 37 °C for 10 min. PLTs were centrifuged at 1,000g for 10 min to concentrate barbell-proPLTs/circular-prePLTs, and the resultant PLT pellet was washed briefly and then resuspended in PLT resuspension buffer (10 mM HEPES, 140 mM NaCl, 3 mM KCl, 0.5 mM  $\text{MgCl}_2$ , 5 mM  $\text{NaHCO}_3$ , 10 mM glucose, pH 7.4).

**Flow cytometry.** Washed PLTs/PPLTs were collected from whole blood and examined under resting conditions. Samples were probed with FITC-conjugated antibodies against CD61, and PE-conjugated antibodies against CD62P (Beckton Dickinson, Franklin Lakes, NJ) and run on a FACSCalibur flow cytometer (Beckton Dickinson). PLTs/PPLTs were gated by their characteristic forward- and side-scattering as they passed through the detector, and their total fluorescence intensity was calculated after subtraction of a FITC- or PE-conjugated IgG antibody specificity control (Beckton Dickinson). Analysis of PLT/PPLT mean fluorescence intensity was performed for at least three different samples. Error bars represent 1 s.d. about the mean for at least 3 independent samples.

**Electron microscopy.** For thin-section electron microscopy, human PLTs were fixed with 1.25% paraformaldehyde, 0.03% picric acid, 2.5% glutaraldehyde in

0.1-M cacodylate buffer (pH 7.4) for 1 h, post-fixed with 1% osmium tetroxide, dehydrated through a series of alcohols, infiltrated with propylene oxide, and embedded in epoxy resin. Ultrathin sections were stained and examined with a Tecnai G2 Spirit BioTwin electron microscope (Hillsboro, OR) at an accelerating voltage of 80 kV. Images were recorded with an Advanced Microscopy Techniques (AMT) 2-K charged coupled device camera, using AMT digital acquisition and analysis software (Advanced Microscopy Techniques, Danvers, MA). For negative stain electron microscopy, samples were fixed with 0.25% formaldehyde, lysed in 60 mM Pipes, 25 mM Hepes, 10 mM EGTA, 2 mM  $\text{MgCl}_2$  (PHEM buffer) containing 0.5% Triton X-100, and immediately centrifuged on the surface of carbon-formar-coated copper grids at 280 g. Grids were stained with 1% uranyl acetate, and viewed in a JEOL 1200 electron microscope at an accelerating voltage of 60 kV.

**Drug treatments.** Samples were incubated with 5  $\mu\text{M}$  nocodazole (Sigma-Aldrich, St. Louis, Missouri, USA), 2.5  $\mu\text{M}$  latrunculin, 10  $\mu\text{M}$  cytochalasin D, 5  $\mu\text{M}$  jasplakinolide (Invitrogen) or DMSO (vector control, Sigma-Aldrich) for up to 6 h at 37 °C.

**Preparation of photomicrographs.** The digital images produced in Metamorph were assembled into composite images by using ImageJ and Adobe Photoshop CS3 (Adobe Systems, San Jose, CA). Dividing lines explicitly separate different images, or separate regions of the same image. No specific features within an image were enhanced, obscured, moved, removed, or introduced, and adjustments made to the brightness, contrast, and colour balance were linearly applied to the whole image.

## References

- Nurden, A. T. Qualitative disorders of platelets and megakaryocytes. *J. Thromb. Haemost.* **3**, 1773–1782 (2005).
- Choi, E. S., Nichol, J. L., Hokom, M. M., Hornkohl, A. C. & Hunt, P. Platelets generated *in vitro* from proplatelet-displaying human megakaryocytes are functional. *Blood* **85**, 402–413 (1995).
- Italiano, J. E. Jr, Lecine, P., Shivdasani, R. A. & Hartwig, J. H. Blood platelets are assembled principally at the ends of proplatelet processes produced by differentiated megakaryocytes. *J. Cell Biol.* **147**, 1299–1312 (1999).
- Leven, R. M. Megakaryocyte motility and platelet formation. *Scanning Microsc.* **1**, 1701–1709 (1987).
- Tablin, F., Castro, M. & Leven, R. M. Blood platelet formation *in vitro*. The role of the cytoskeleton in megakaryocyte fragmentation. *J. Cell Sci.* **97**(Pt 1), 59–70 (1990).
- Italiano, J. E. Jr, Patel-Hett, S. & Hartwig, J. H. Mechanics of proplatelet elaboration. *J. Thromb. Haemost.* **5**(Suppl 1), 18–23 (2007).
- Thon, J. N. *et al.* Cytoskeletal mechanics of proplatelet maturation and platelet release. *J. Cell Biol.* **191**, 861–874 (2011).
- Kraytman, M. Platelet size in thrombocytopenias and thrombocytosis of various origin. *Blood* **41**, 587–598 (1973).
- Behnke, O. & Forer, A. From megakaryocytes to platelets: platelet morphogenesis takes place in the bloodstream. *Eur. J. Haematol. Suppl.* **61**, 3–23 (1998).
- Tong, M., Seth, P. & Penington, D. G. Proplatelets and stress platelets. *Blood* **69**, 522–528 (1987).
- Jurak Begonja, A., Hoffmeister, K. M., Hartwig, J. H. & Falet, H. FlnA-null megakaryocytes prematurely release large and fragile platelets that circulate poorly. *Blood* **118**, 10 (2011).
- Schwartz, H. *et al.* Anucleate platelets generate progeny. *Blood* **115**, 8 (2010).
- McDonald, T. P. A comparison of platelet size, platelet count, and platelet 35S incorporation as assays for thrombopoietin. *Br. J. Haematol.* **34**, 257–267 (1976).
- Patel-Hett, S. *et al.* The spectrin-based membrane skeleton stabilizes mouse megakaryocyte membrane systems and is essential for proplatelet and platelet formation. *Blood* **118**, 11 (2011).
- Howell, W. H. & Donahue, D. D. The production of blood platelets in the lungs. *J. Exp. Med.* **65**, 177–203 (1937).
- White, J. G. & Sauk, J. J. The organization of microtubules and microtubule coils in giant platelet disorders. *Am. J. Pathol.* **116**, 514–522 (1984).
- Falet, H. *et al.* A novel interaction between FlnA and Syk regulates platelet ITAM-mediated receptor signaling and function. *J. Exp. Med.* **207**, 1967–1979 (2011).
- Hartwig, J. H. & Italiano, J. E. Jr. Cytoskeletal mechanisms for platelet production. *Blood Cells Mol. Dis.* **36**, 99–103 (2006).
- Gresele, P. *et al.* Dominant inheritance of a novel integrin beta3 mutation associated with a hereditary macrothrombocytopenia and platelet dysfunction in two Italian families. *Haematologica* **94**, 663–669 (2009).
- Chen, Z. *et al.* The May-Hegglin anomaly gene MYH9 is a negative regulator of platelet biogenesis modulated by the Rho-ROCK pathway. *Blood* **110**, 171–179 (2007).
- Chen, Z. & Shivdasani, R. A. Regulation of platelet biogenesis: insights from the May-Hegglin anomaly and other MYH9-related disorders. *J. Thromb. Haemost.* **7** (Suppl 1), 272–276 (2009).

22. Hartwig, J. H. & DeSisto, M. The cytoskeleton of the resting human blood platelet: structure of the membrane skeleton and its attachment to actin filaments. *J. Cell Biol.* **112**, 407–425 (1991).
23. Hoffmeister, K. M. *et al.* The clearance mechanism of chilled blood platelets. *Cell* **112**, 87–97 (2003).
24. Patel-Hett, S. *et al.* Visualization of microtubule growth in living platelets reveals a dynamic marginal band with multiple microtubules. *Blood* **111**, 4605–4616 (2008).
25. Italiano, J. E. Jr *et al.* Mechanisms and implications of platelet discoid shape. *Blood* **101**, 4789–4796 (2003).
26. Pozarowski, P., Holden, E. & Darzynkiewicz, Z. Laser scanning cytometry: principles and applications. *Methods Mol. Biol.* **319**, 165–192 (2006).

### Acknowledgements

This work was supported in part by the National Institutes of Health grant HL68130 (J.E.I.) and NSF grant DMS-1118206 (A.M.). J.E.I. is an American Society of Hematology Junior Faculty Scholar. J.N.T. is an American Society of Hematology Scholar. We acknowledge the staff at CompuCyte for access to their laser scanning cytometer and support in building the analysis modules described in this manuscript; and Dr. Hervé Falet at Harvard Medical School for access to his Filamin A KO mice.

### Author contributions

J.N.T. designed and performed the experiments, analysed the data and wrote the manuscript; H.M. performed many of the blood smear, immunofluorescence microscopy, and flow cytometry experiments. A.B. performed the Filamin A KO experiments. J.H.H. designed and performed the thin section and negative stain electron microscopy experiments, and contributed to writing the manuscript. J.E.I. helped design the experiments, analyse the data, and contributed to writing the manuscript. J.Z., K.C.L. and A.M. developed the computational model and contributed to writing the manuscript.

### Additional information

**Supplementary Information** accompanies this paper at <http://www.nature.com/naturecommunications>

**Competing financial interests:** The authors declare no competing financial interests.

**Reprints and permission** information is available online at <http://npg.nature.com/reprintsandpermissions/>

**How to cite this article:** Thon, J. N. *et al.* Microtubule and cortical forces determine platelet size during vascular platelet production. *Nat. Commun.* 3:852 doi: 10.1038/ncomms1838 (2012).

## Online Supplementary Material

Supplementary Computational Model online.

Supplementary RBC Lysis online.

### **Supplementary Figure 1. Laser scanning cytometry analysis work flow used to quantify intermediates in PLT production from whole blood samples.**

Human whole blood was collected from healthy volunteers and PRP isolated by centrifugation. PLTs were subsequently spun down onto poly-L-lysine-coated glass coverslides, fixed, permeabilized, and probed for  $\beta$ 1-tubulin. **Figure a/b:** Laser scanning cytometry analysis work flow for the detection and quantification of intermediates in PLT production from PRP. Graphical modules represent analysis protocols that initially scan coverslides at 20x magnification (mosaic scan) to generate a low resolution DIC and fluorescence image map of the sample slide (Fig. b, *top*). Fifty '5x5' regions of interest (denoted by the blue squares) were selected for each coverslide and scanned using a 60x objective (field scan) to generate fluorescence region maps (Fig. b, *middle*) composed of 25 high resolution images (Fig. b, *bottom*). These were processed using manufacturer-developed modules to threshold individual objects based on known human PLT parameters and contour these events for subsequent quantitative analysis. **Figure c:** Data were subject to morphological and signal-level dependent scattergram analysis, and barbell-proPLTs, figure '8' proPLTs, circular-prePLTs, resting PLTs and activated PLTs were gated based on a combination of parameters. **Figure d:** Representative galleries of cells from the aforementioned gated regions. For the purposes of exactness in all subsequent quantifications, figure '8' proPLTs, activated PLTs, and PLT clumps were excluded from the analysis.

**Supplementary Figure 2. Giemsa-stained blood smears and IF microscopy of fixed barbell-proPLTs that were concentrated from human whole blood following RBC lysis.**

Giemsa-stained blood smears were generated from human whole blood directly, or following fixation with 1% and 0.1% formaldehyde, RBCs lysis, and sample concentration. **Figure a:** Representative blood smears demonstrate the presence of barbell-proPLTs, circular-prePLTs, and discoid PLTs prior to and following RBC lysis. Fixation with 0.1% formaldehyde before RBC lysis resulted in minor PLT swelling, the disappearance of barbell-proPLTs, and appearance of greater numbers of circular-prePLTs. Representative examples of discoid PLTs are indicated by black arrows, while circular-prePLTs or barbell-proPLTs are indicated by white arrows. **Figure b:** Human whole blood PLT fixed with 1% formaldehyde did not demonstrate swelling relative to those in untreated PRP controls, and remained normally distributed about their mean area. **Figure c:** Barbell-proPLTs could be isolated from whole blood following RBC lysis, and concentrated by differential centrifugation. Samples were probed with antibodies against the PLT-specific marker GPIIIa and examined by IF microscopy to reveal long proPLTs not usually detected in PRP. Representative examples of discoid PLTs are indicated by black arrows, while circular-prePLTs or barbell-proPLTs are indicated by white arrows.

**Supplementary Figure 3. Flow cytometric analysis of fixed human whole blood PLTs and PLT intermediates following RBC lysis.**

**Figure a:** Flow cytometric analysis of human washed PLTs and whole blood PLTs following 1% formaldehyde fixation and RBC lysis (**Fig. b**) demonstrate the presence of GPIIIa positive objects with forward- and side-scatter dimensions larger than those of discoid PLTs (PPLT gate). **Figure c:** These were shown not to be comprised of PLT aggregates (differential interference

contrast image, *left*) and remained resting following RBC lysis, as determined by the lack of CD62P activation on their surface (*right*).

**Supplementary Figure 4. Immunofluorescence and negative stain electron microscopy of human whole blood barbell-proPLTs, circular-prePLTs, human/mouse discoid PLTs, and mouse proPLT culture intermediates.**

**Figure a/c/e:** Human (Fig. a) whole blood barbell-proPLTs, circular-prePLTs, and discoid PLTs were spun down onto poly-L-lysine coated glass coverslides, fixed, permeabilized, and probed for  $\beta$ 1-tubulin. Linescans were drawn across the marginal coils of these structures (represented in yellow) and used to measure the size and fluorescence intensity of the peripheral microtubule cytoskeleton. These were compared to mouse whole blood PLTs from WT and Day 4 RAMPS-treated mice (Fig. c) and barbell-proPLT and circular-prePLT intermediates from mouse FLC cultures (Fig. e). These did not reveal any difference in the thickness or fluorescence intensity of the microtubule ring, and suggest that the number of microtubule coils in these structures is equivalent. Discoid PLTs from Filamin A KO mice were used as a positive control to demonstrate that differences in microtubule band thickness and fluorescent intensity could be resolved using this approach. **Figure b/d/f:** Barbell-proPLTs and circular-prePLTs were concentrated from human whole blood following fixation with 1% formaldehyde, RBC lysis, and differential centrifugation. These were analyzed by negative stain electron microscopy and compared to mouse whole blood PLTs from WT and Day 4 RAMPS-treated mice (Fig. d) and barbell-proPLT and circular-prePLT intermediates from mouse FLC cultures (Fig. f). Direct visualization and precise counting of individual microtubules along the periphery of the cell revealed values of between 6-8 individual microtubules for discoid PLTs, and their numbers and

arrangement were not significantly different in barbell-proPLTs or circular-prePLTs from the same donor or between donors. Discoid PLTs from Filamin A KO mice were used as a positive control to demonstrate that differences in microtubule band thickness and microtubule count could be resolved using this approach. Negative stain electron microscopy did not reveal any difference in the localization, thickness, fluorescence intensity, or microtubule number of the marginal microtubule band between the samples compared. These observations suggest that circular-prePLTs identified in human whole blood and thrombocytopenic mice are structurally equivalent to circular-prePLTs observed in mouse FLC cultures, and likely represent an intermediate stage in PLT production *in vivo*.

**Supplementary Figure 5. Quantification of resting (discoid) PLTs, circular-prePLTs, and barbell-proPLTs in human/mouse whole blood 0 and 6 hours post-collection.**

**Figure a:** PRP was isolated from human whole blood by centrifugation, and stored at 22°C with 5% CO<sub>2</sub> and gentle rotation in a humidified incubator for 0 and 6 hours. PLTs were subsequently spun down onto poly-L-lysine-coated glass coverslides, fixed, permeabilized, and probed for  $\beta$ 1-tubulin. Objects are displayed as a density scattergram with maximum pixel intensity plotted along the y-axis, and area ( $\mu\text{m}^2$ ) plotted along the x-axis. Discoid PLTs are represented by the cyan box (R3) and the blue box (R2) represents circular-prePLTs. **Figure b:** Resting PLT, circular-prePLT and barbell-proPLT counts were quantified and normalized for total object counts. At 22°C, relative discoid PLT counts smaller than 3 $\mu\text{m}$  in diameter do not change during cell culture. While barbell-proPLT numbers increased significantly after 6 hours, these were lower than PRP cultured at 37°C for the same period of time (Fig. 5). **Figure c:** Human whole blood was collected directly into Sodium Citrate, EDTA, and Heparin tubes and either stored in

the same tube for 6 hours at 37°C or transferred into a new anticoagulant-treated tube every hour. Representative immunofluorescence microscopy images of  $\beta$ 1-tubulin-stained PRP from anticoagulant-treated human whole blood demonstrate the presence of barbell-proPLTs in Sodium Citrate tubes after 6 hours in both singly-treated and hourly-treated samples. While barbell-proPLTs were evident in EDTA- and Heparin-treated blood that had been stored for 6 hours after only a single treatment with the anticoagulant, these were absent in hourly-treated samples and suggest that this effect is transient. Representative examples of barbell-proPLTs are indicated by white arrows. **Figure d:** PRP was collected from WT and RAMPS-treated mice on Day 4 post-infusion and cultured at 37°C with 5% CO<sub>2</sub> and gentle rotation in a humidified incubator for 0 and 6 hours. Representative immunofluorescence microscopy images of  $\beta$ 1-tubulin-stained PRP reveal larger PLTs and greater numbers of barbell-proPLTs (white arrows) in RAMPS-treated mice versus the WT controls.

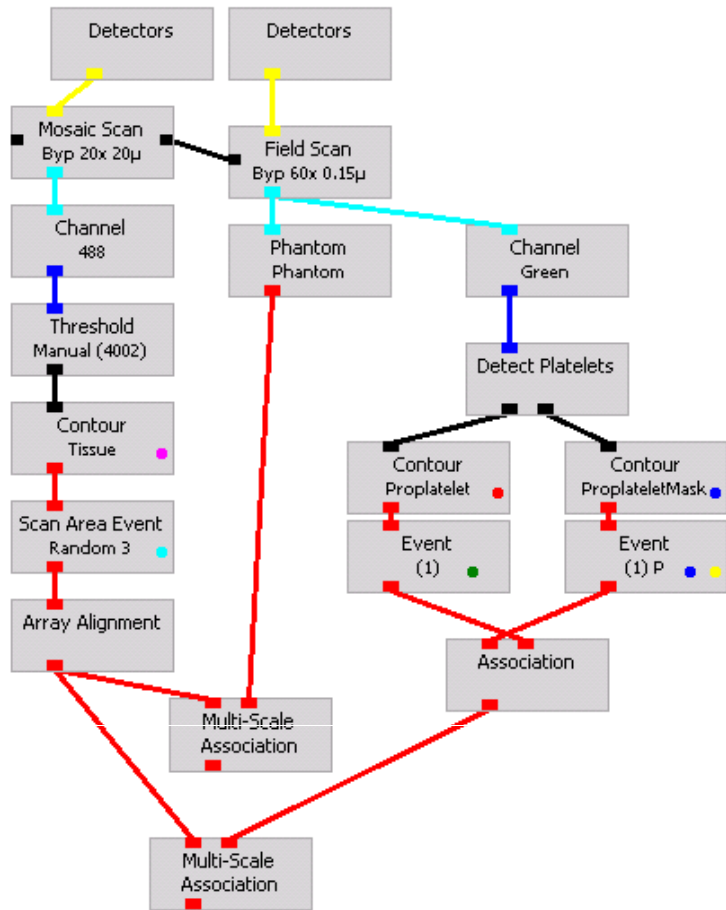
### **Supplementary Figure 6. Mathematical modeling of barbell-proPLT conversion.**

**Figure a:** Simulated shapes of a proPLT in the case cell area are conserved by cortex tension. Cell interior is in gray. From top to bottom: the ratio of the shown cell perimeter to the initial, circular, perimeter  $L/L_0=1, 1.5, 2$ . **Figure b:** Value of the computed pressure required for maintaining the area of a proPLT. The corridor forms at  $1.8 < L/L_0 < 2$  (in this region shown by cyan, the necessary pressure increases) beyond which the corridor has a minimum width of 0.2  $\mu$ m. **Figure c:** Bending energy of the microtubule-bundle. Solid line: simulation results. Red circles: results from analytical approach for the initial stage of the proPLT formation. The energy increases when the corridor forms (shown by cyan), after which the energy remains constant. **Figure d:** Simulated force along the microtubule-bundle. Solid line: maximum force. Dashed

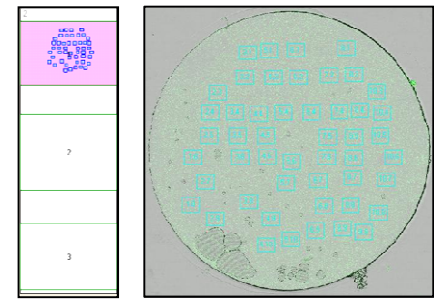
line: average force. Dotted line: minimum force. The maximal force decreases initially, then increases to the initial level during the corridor formation (shown by cyan), and then remains constant. Note from the scaling that the force is inversely proportional to the square of the initial cell perimeter. **Figure e:** Simulated PLT diameter vs. effective external pressure generated by the cortex tension. **Figure f:** Energy of the twisted bundle of two MTs as a function of the helical pitch. The energy minimum corresponds to the predicted pitch of the twisted MT bundle. In the calculation, the following parameters were used:  $Yl_p k_B T = 28 \text{ pN} \cdot \mu\text{m}$ ,  $r = 0.1 \mu\text{m}$ ,  $J = 2000 \text{ pN}$ .

# Supplementary Figure 1

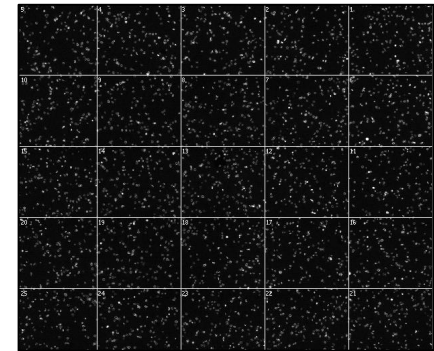
## a. hPRP Scanning Cytometry Analysis Work Flow



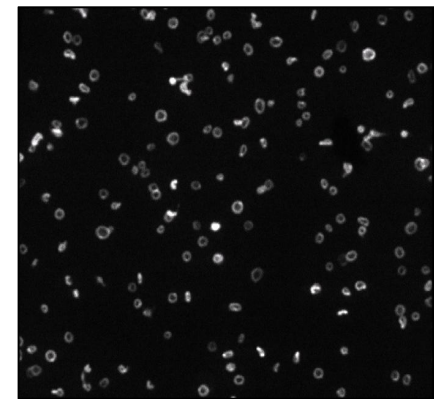
## b. hPRP - Coverslide



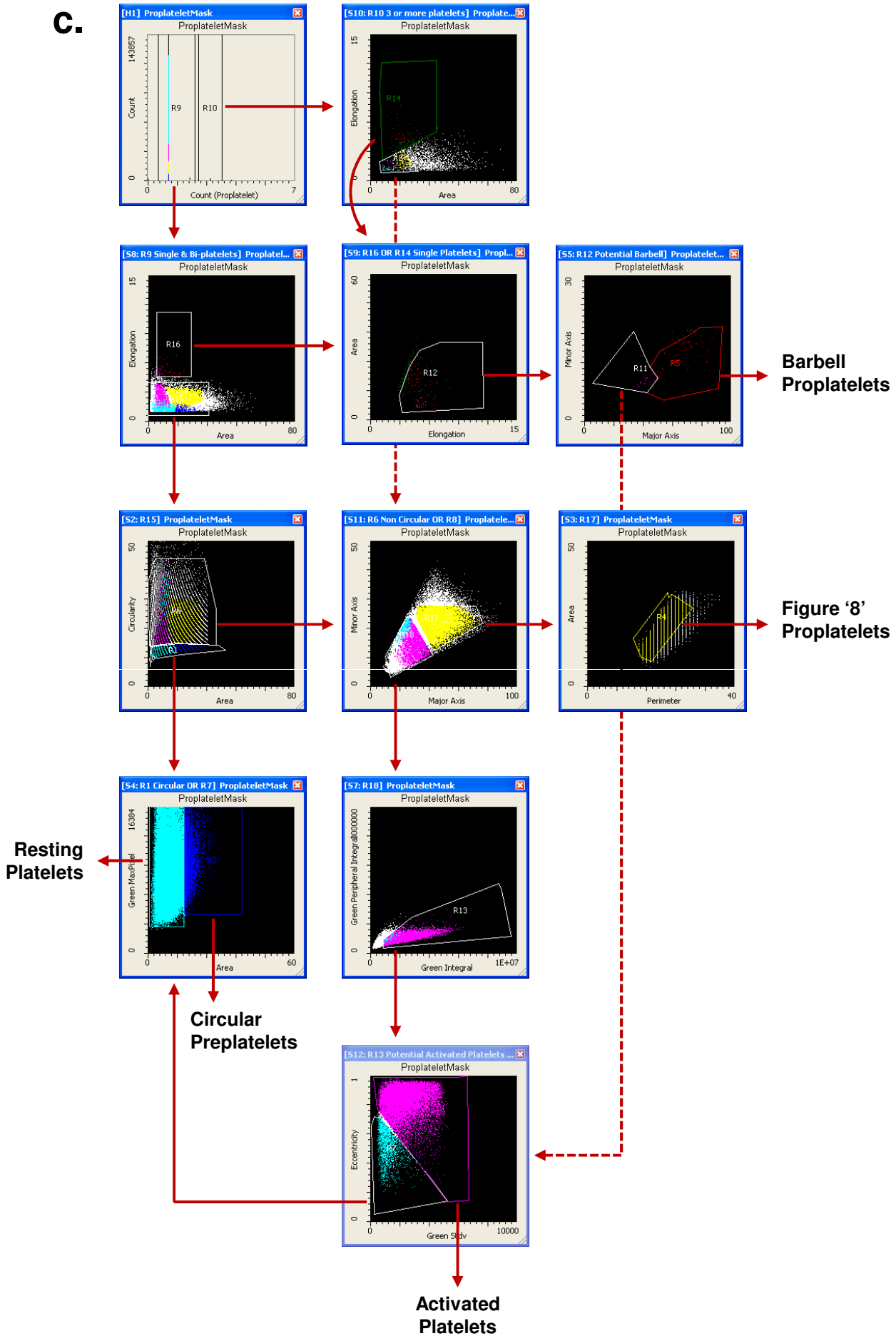
hPRP - Region



hPRP - Image

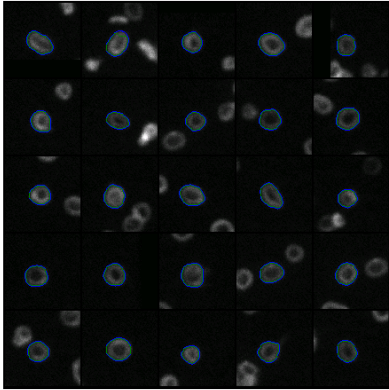


C.

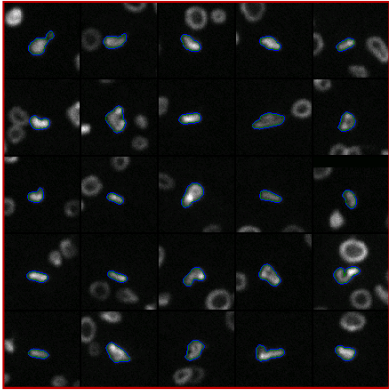


**d.**

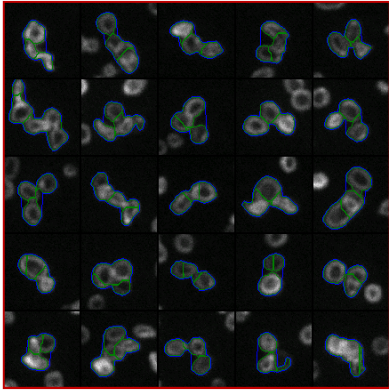
**Resting Platelets**



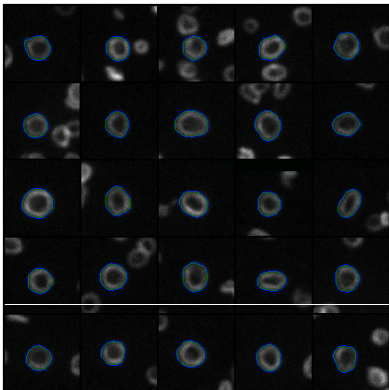
**\*Activated Platelets**



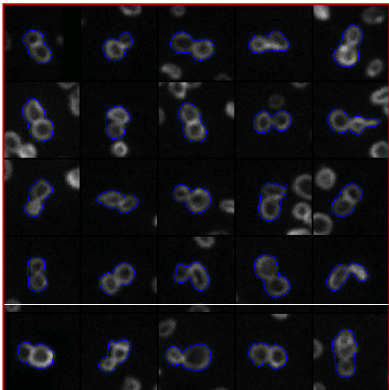
**\*Platelet Clumps**



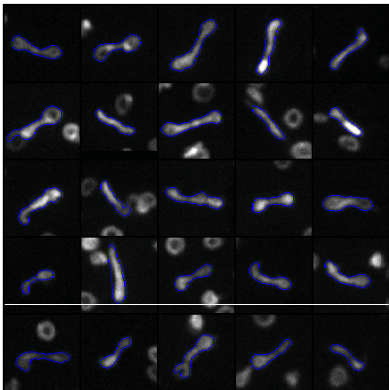
**Circular Proplatelets**



**\*Figure '8' Proplatelets**

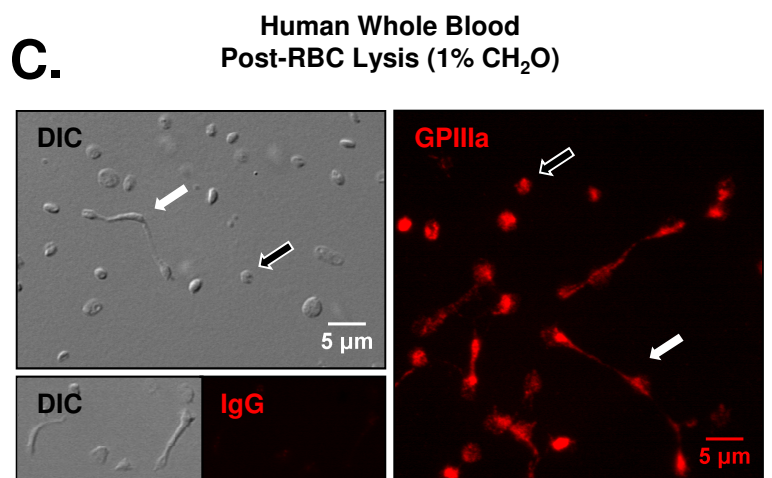
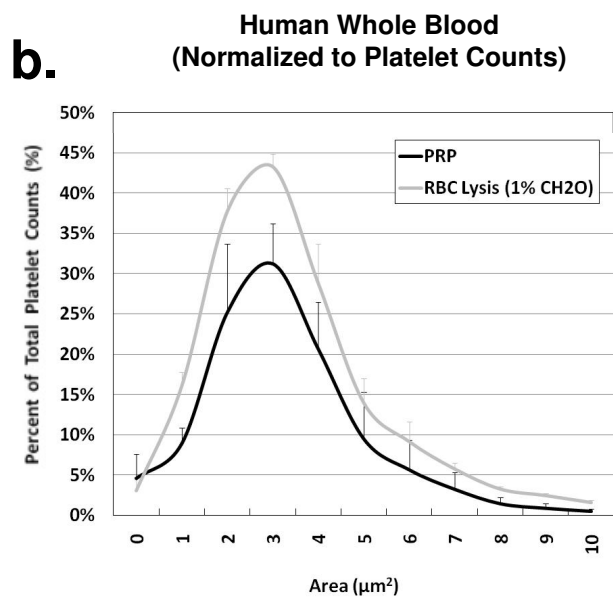
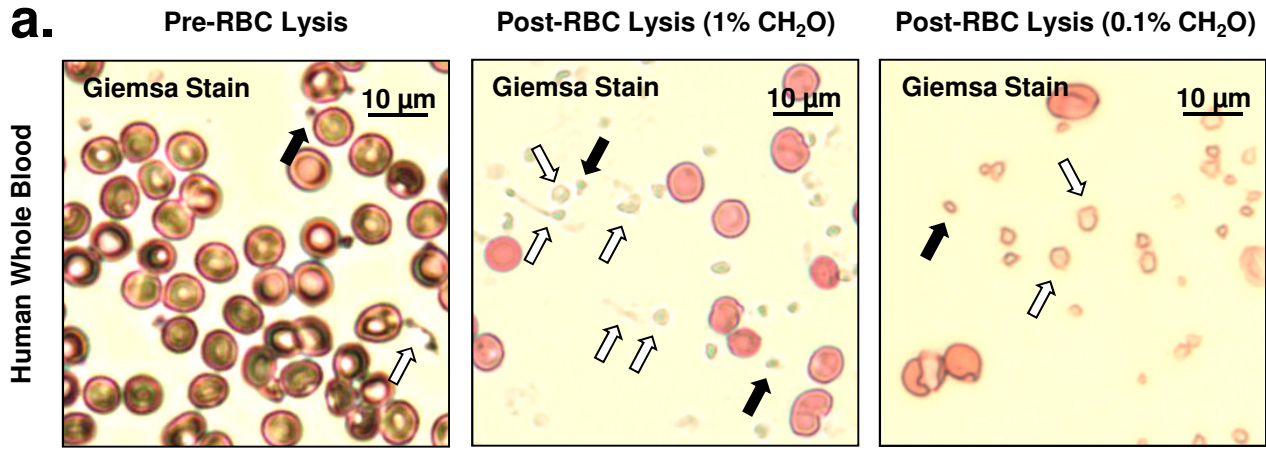


**Barbell Proplatelets**



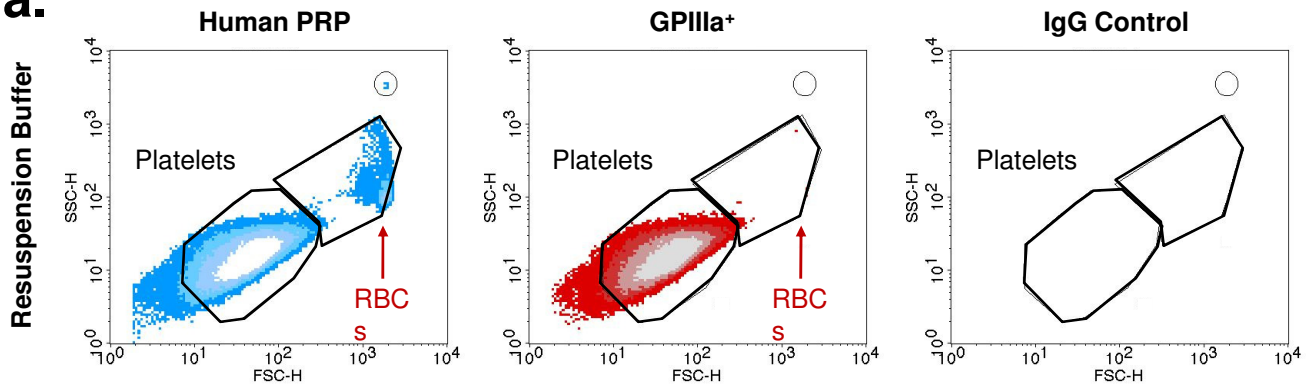
**\*Excluded from quantification**

# Supplementary Figure 2

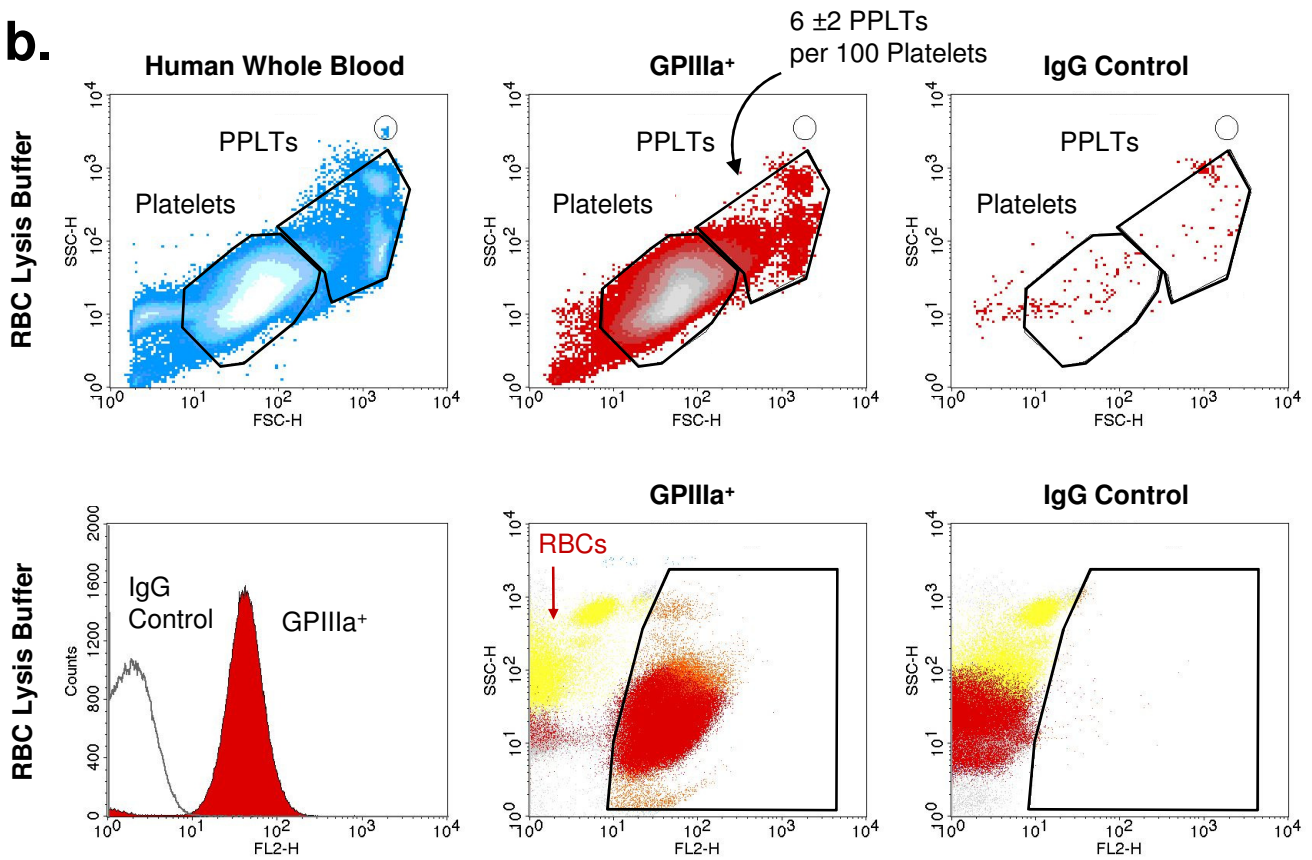


# Supplementary Figure 3

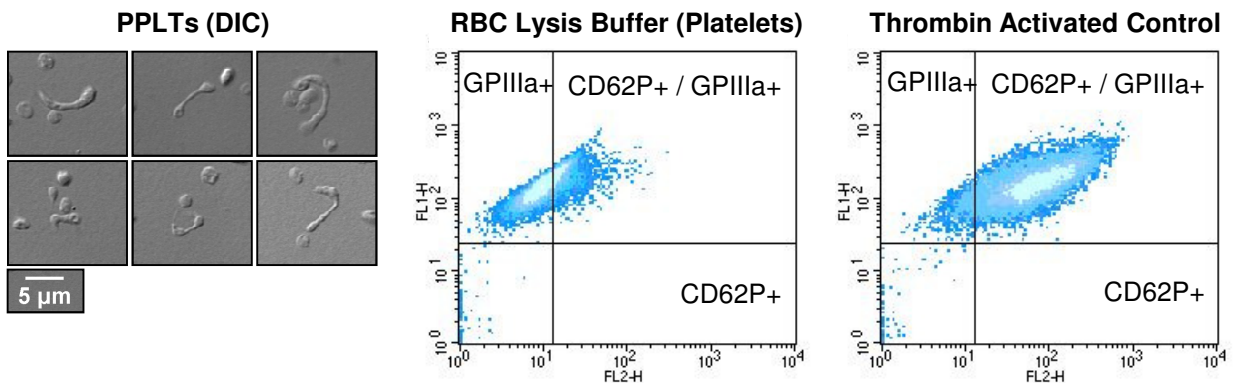
**a.**



**b.**

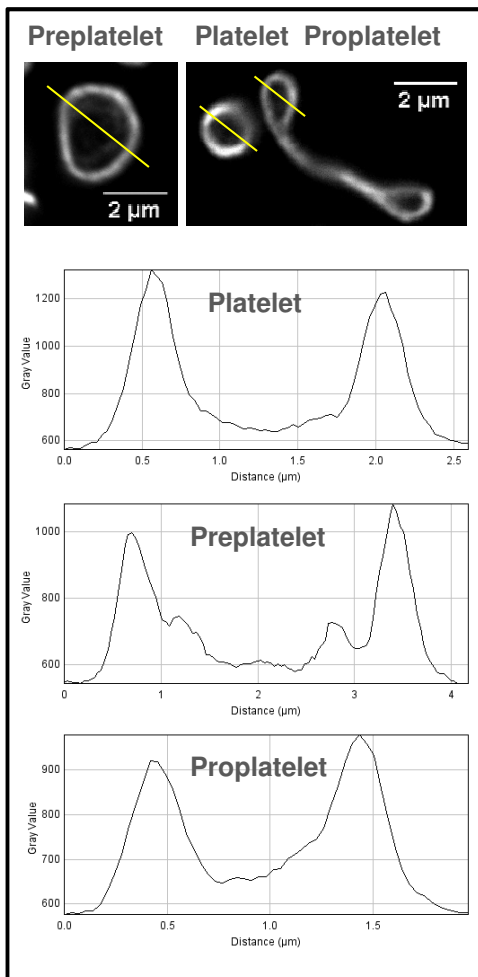


**c.**

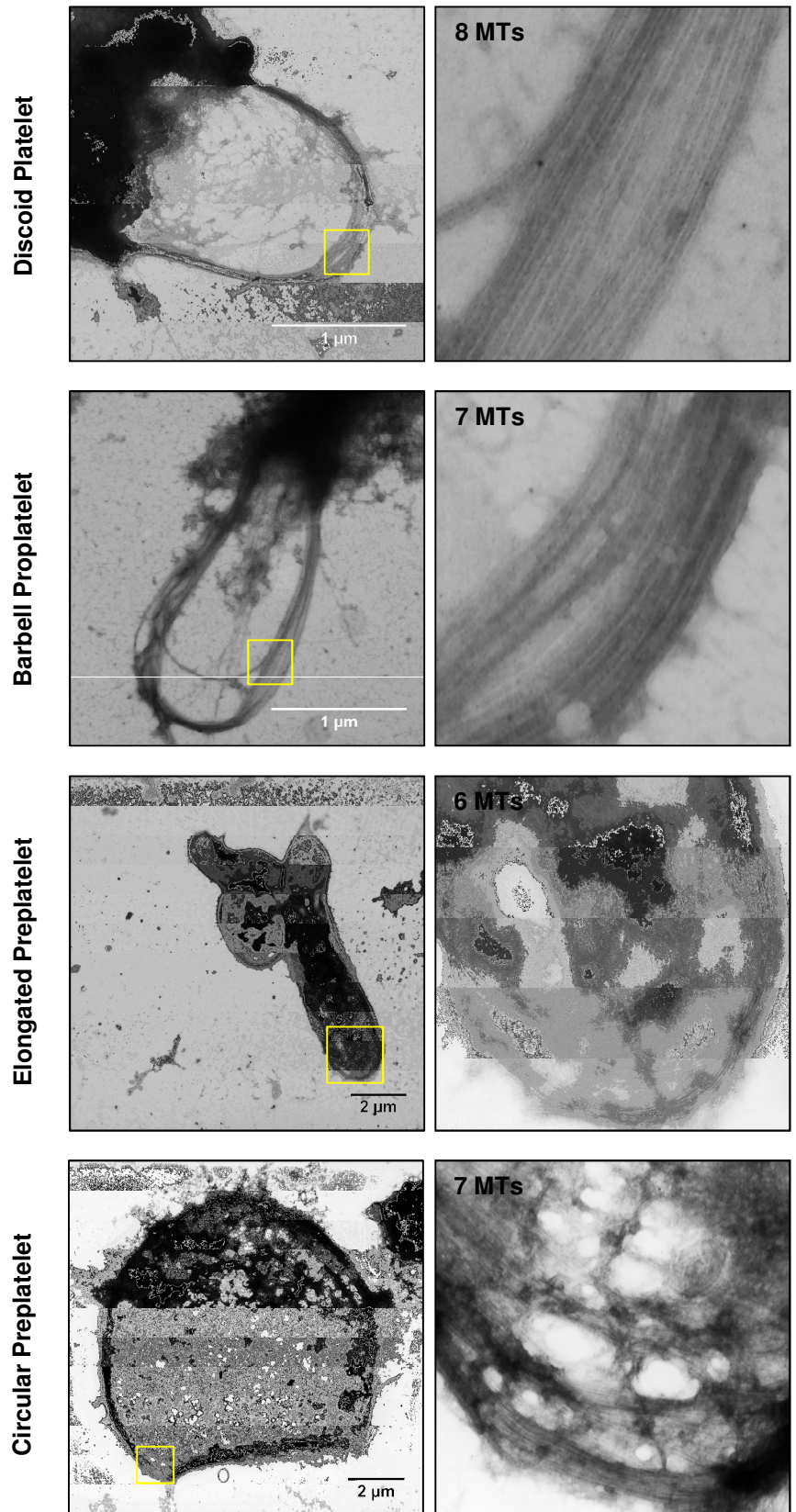


# Supplementary Figure 4

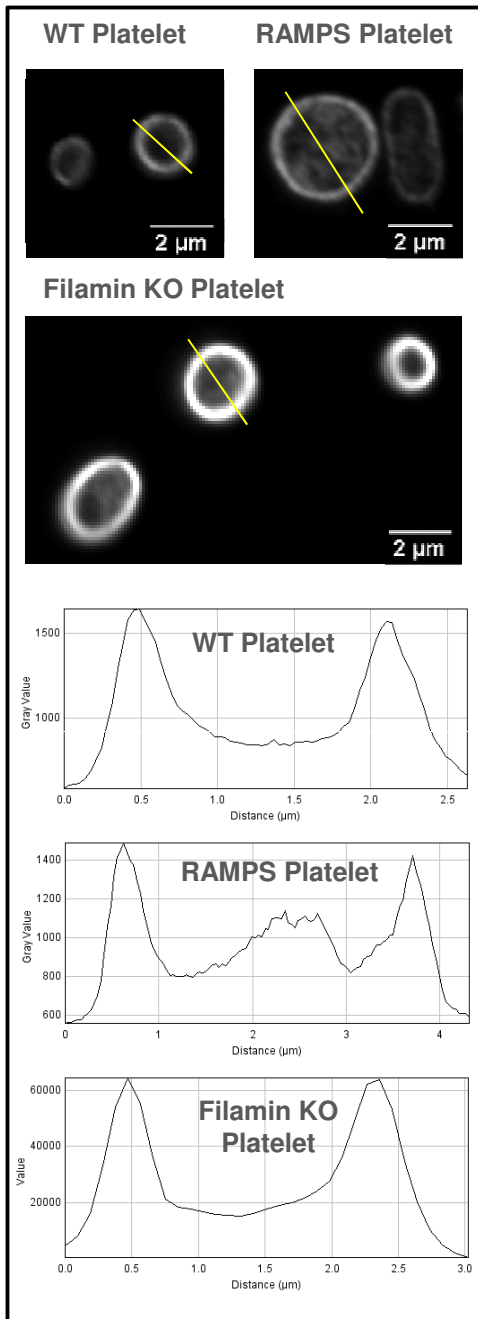
## a. Human Whole Blood



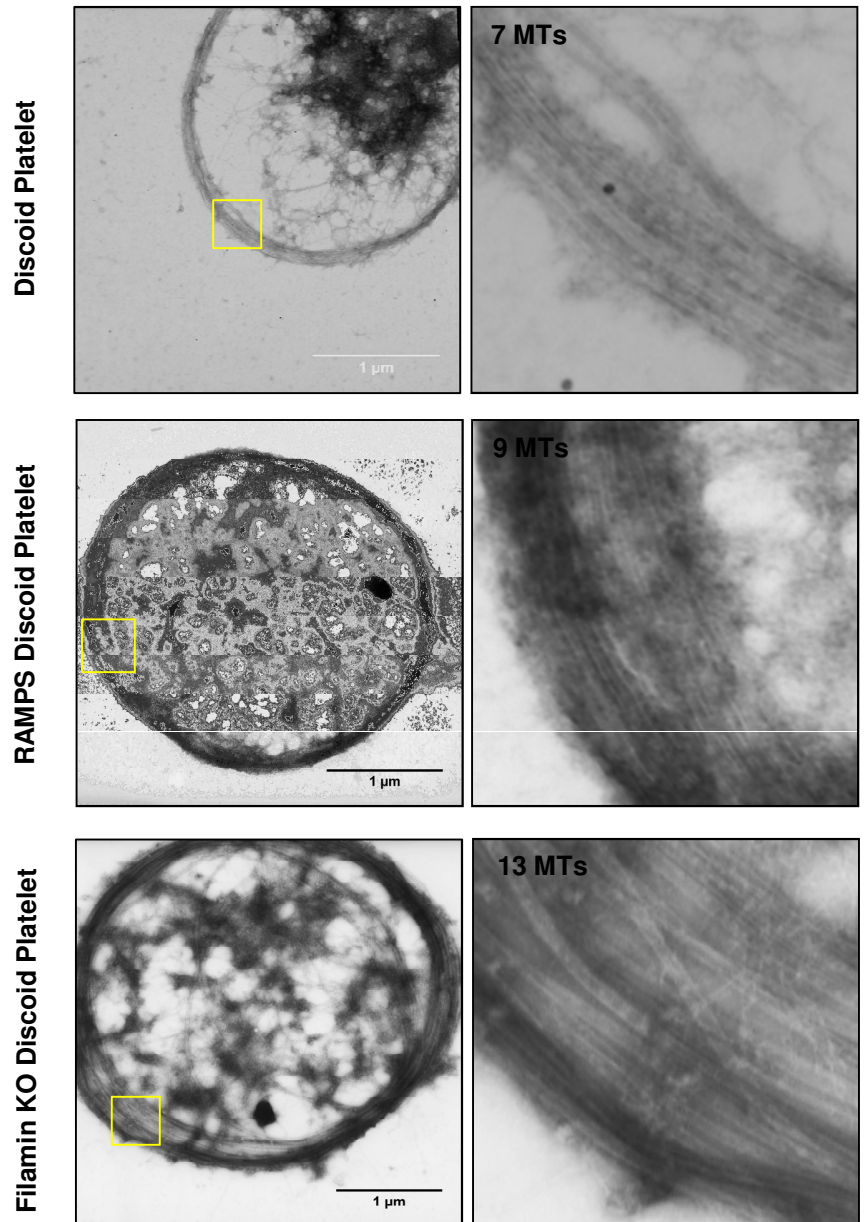
## b. Human Whole Blood



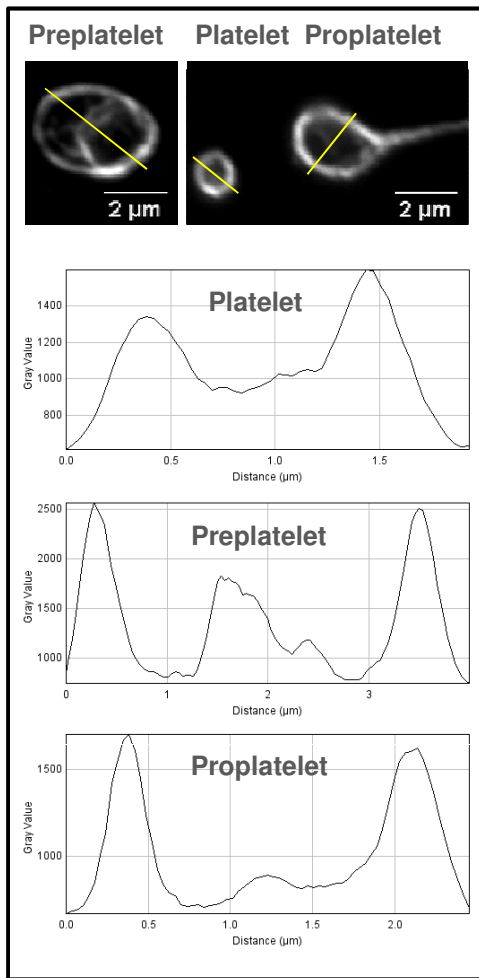
**C. Mouse Whole Blood**



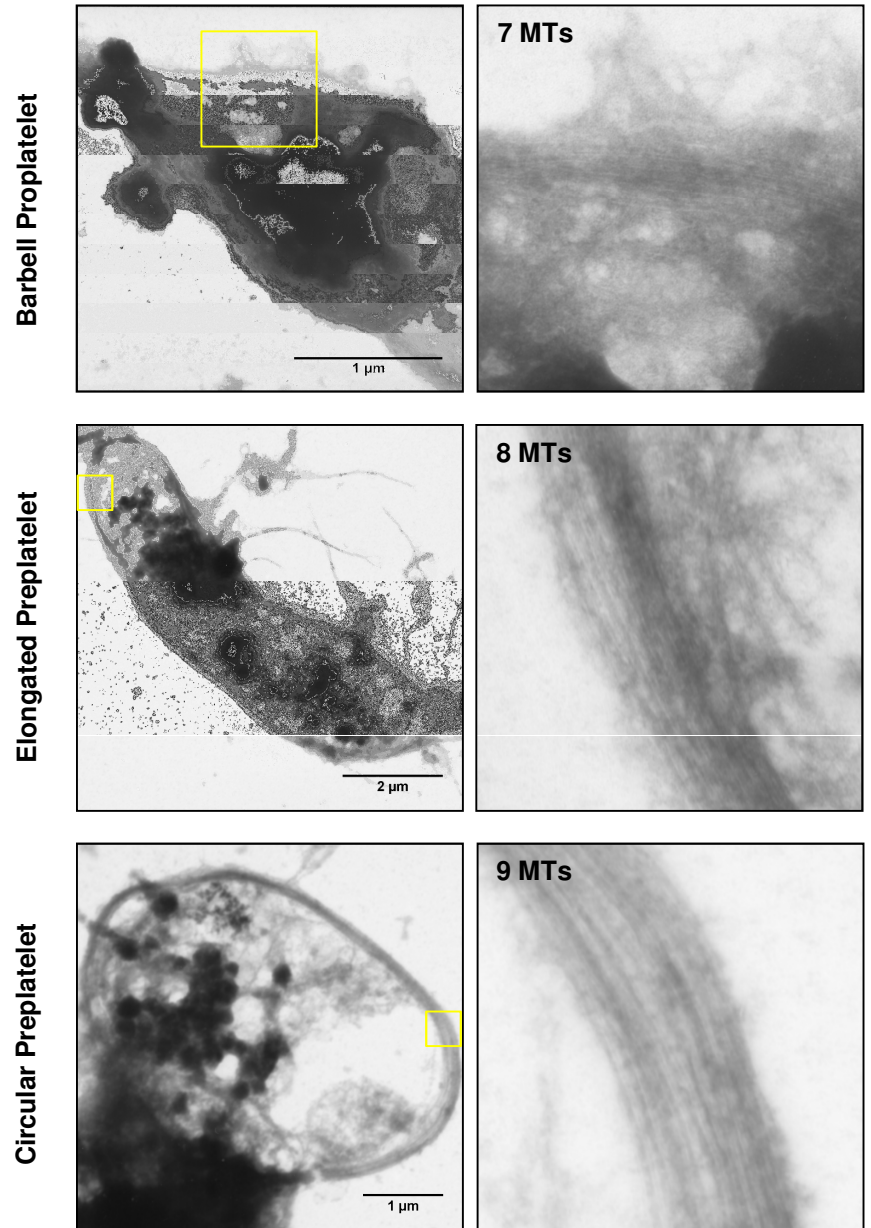
**d. Mouse Whole Blood**



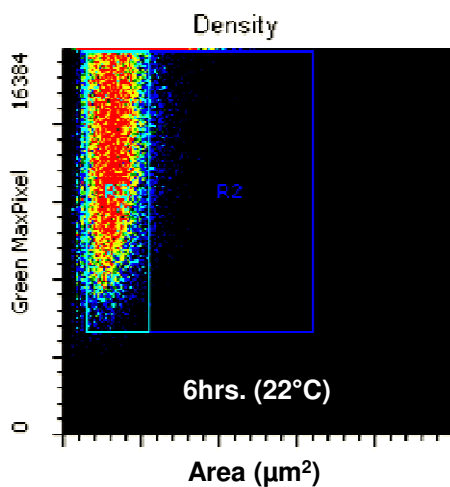
**e. Mouse MK Cell Culture**



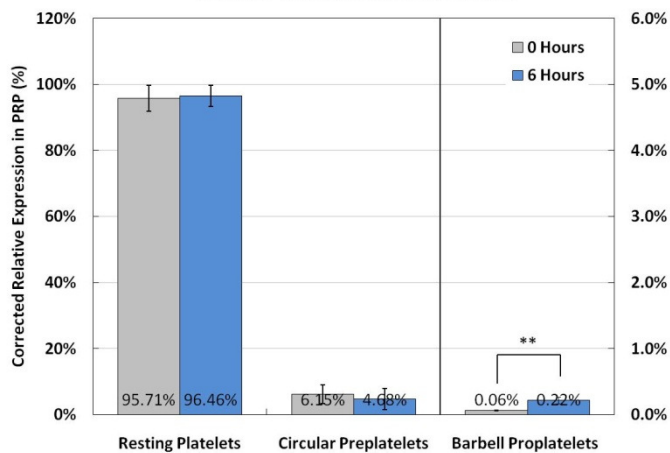
**f. Mouse MK Cell Culture**



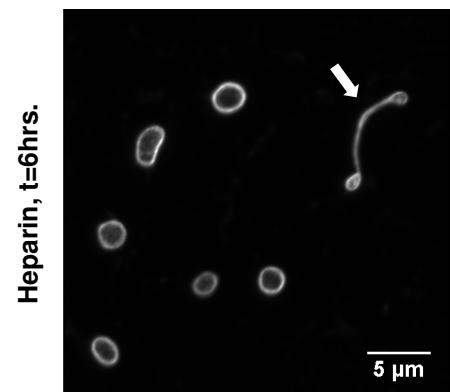
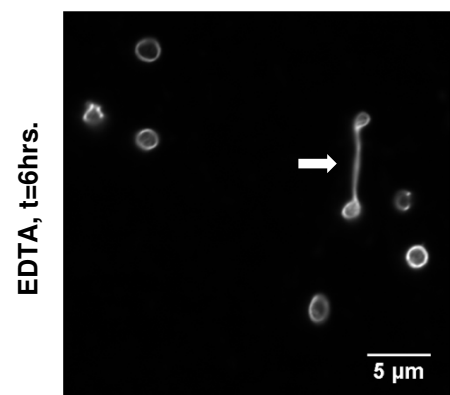
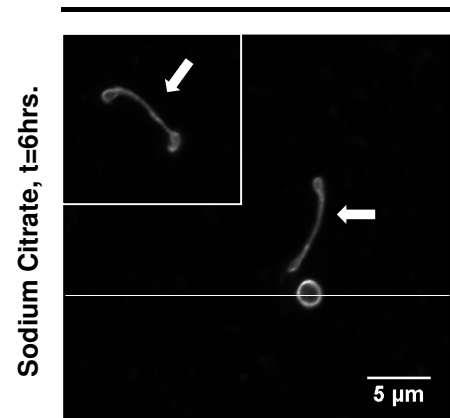
**a.** Human Platelet Rich Plasma



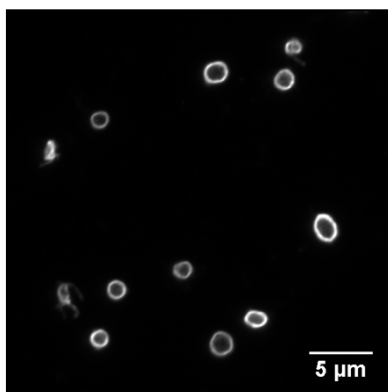
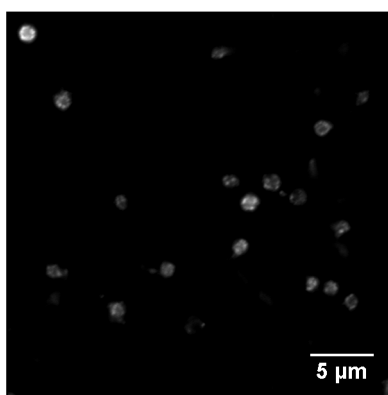
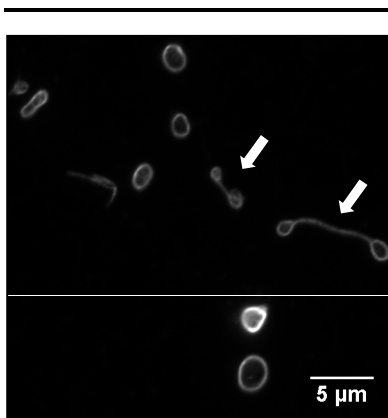
**b.** Human Platelet Rich Plasma at 22°C



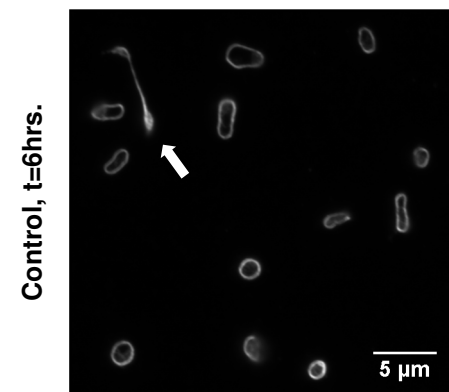
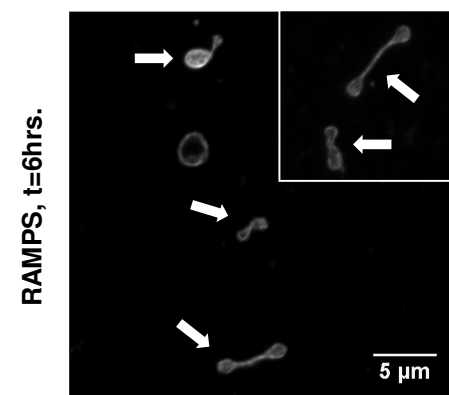
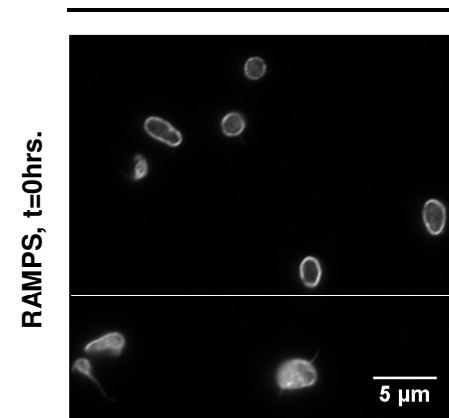
**c.** Single Treatment with Anticoagulant



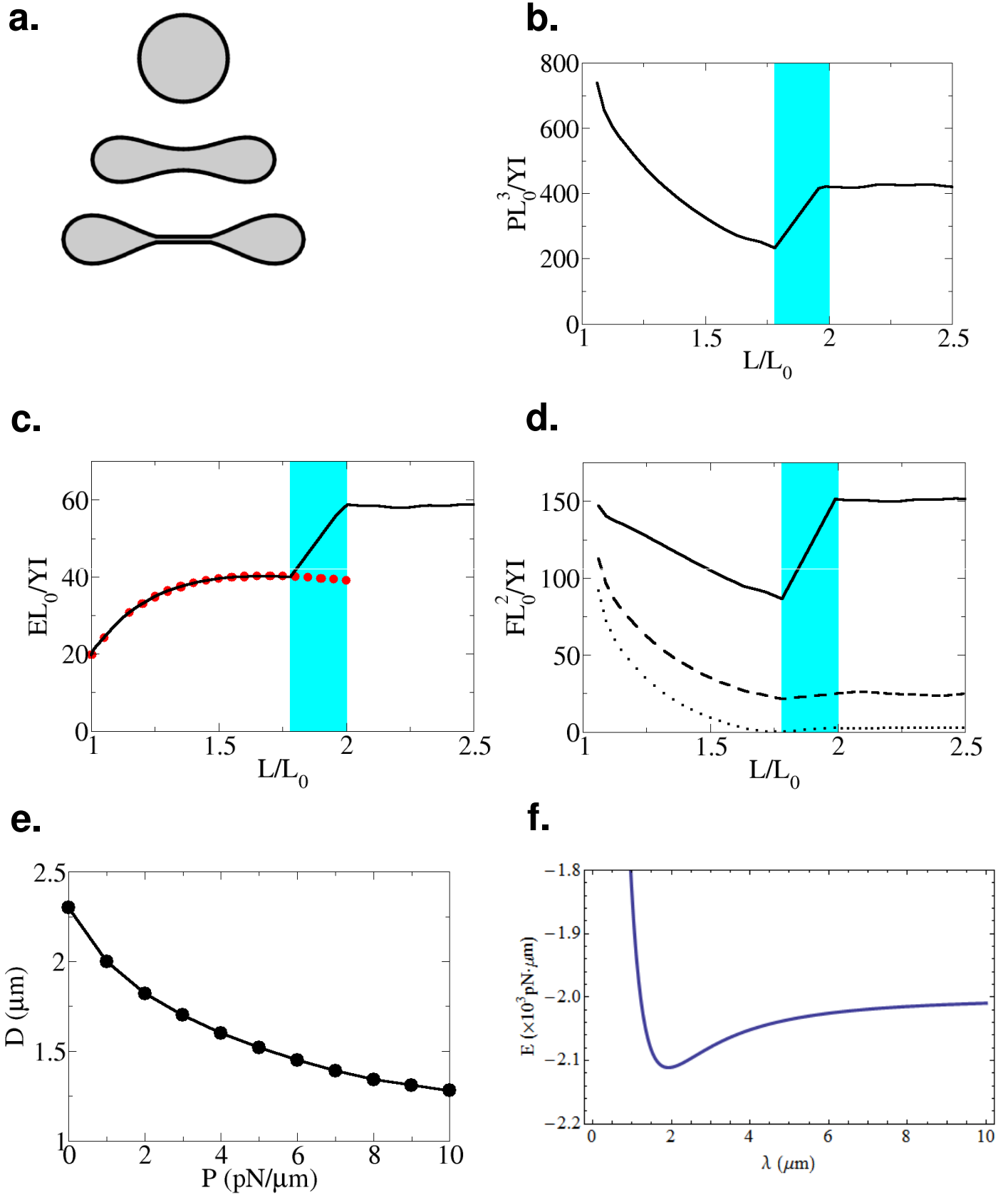
Hourly Treatment with Anticoagulant



**d.** Mouse PRP –  $\beta$ 1-tubulin



# Supplementary Figure 6



## **Computational Model**

We assume that the shape of a proPLT is determined by the microtubule (MT) bundle along its periphery. The MT bundle can be regarded as an elastic loop which keeps extending but maintains a constant thickness (~7 microtubules) during the elongation. Without other forces applied to the elongating MT bundle, the loop will remain circular. Since elongating proPLTs usually form a barbell shape, the deformation of the cell has to be constrained by the external compressive pressure due to the contraction of actin-myosin-spectrin cortex (Fig. 6a). In addition, once the proPLT forms a narrow corridor in the middle, bundling proteins in that region tend to pull the MT bundles on opposite sides together and thus generating a ‘zipping’ force.

We use numerical simulations to investigate how these mechanisms affect the shape of the proPLT. We treat the MT bundle as a node-spring loop. Each node in the loop interacts with its two adjacent neighbors via both stretching and bending forces, and then moves under these forces until all forces are balanced. The loop reaches equilibrium when all the nodes stop moving. The extension of the MT bundle is incorporated by gradually elongating the rest lengths of all the springs in the loop. The compressive force from the actin-myosin-spectrin cortex or from the cytoplasm is included as a pressure on the loop. The bundling proteins in the corridor are treated as transient elastic bonds, which bind to two nearby microtubule-bundles and gradually shrink their bond lengths to cause a ‘zipping’ effect.

## **Simulation procedures**

The spring force on the  $i$ -th node comes from the two adjacent neighbors  $j=i\pm 1$ :

$$\vec{f}_s(i) = k_s \sum_j (r_{i,j} - r_0) \hat{r}_{i,j}, \text{ where } k_s \text{ is the stretching spring constant of each spring,}$$

$r_{i,j} = |\vec{r}_i - \vec{r}_j|$  is the distance from the  $i$ -th node to the  $j$ -th node,  $\hat{r}_{i,j} = (\vec{r}_i - \vec{r}_j) / r_{i,j}$  is the unit vector pointing from  $j$ -th node to  $i$ -th node, and  $r_0$  is the rest length of the springs.

The bending force on node- $i$  has two sources: one is caused by the torque at neighboring nodes  $j=i\pm 1$ , the other is caused by the torque at node  $i$ :

$$\vec{f}_b(i) = \sum_j (\vec{\tau}_j \times \hat{r}_{i,j} / r_{i,j} - \vec{\tau}_i \times \hat{r}_{i,j} / r_{i,j}), \text{ where } \vec{\tau}_i \text{ and } \vec{\tau}_j \text{ are the torques at nodes } i \text{ and } j,$$

respectively. The magnitude of  $\vec{\tau}_i$  is  $\tau_i = k_b \Delta\theta_i$ , where  $k_b$  is the bending spring constant for each node and  $\Delta\theta_i$  is the bending angle at node  $i$ .

The force applied by the external pressure  $P$  to node  $i$  is calculated as  $f_p(i) = P(r_{i,i-1} + r_{i,i+1}) / 2$  and is pointing toward the inside of the cell.

1) If the pressure is caused by the contraction of the actin-myosin-spectrin cortex, the contraction pressure from the cortex should be balanced by the expanding pressure from the bent MT bundle. From Laplace's law, we have  $P = \kappa T$  where  $\kappa$  is the local curvature of the MT bundle and  $T$  is the lateral tension in the cortex.

2) If the pressure is caused by the cell's membrane maintaining its area, we assume that the magnitude of  $P$  is proportional to the change in the area:  $P = P_0(A / A_0 - 1)$ , where  $P_0$  is a constant,  $A$  is current area of the loop and  $A_0$  is the initial area of the loop. The magnitude of  $P_0$  is related to the sensitivity of the area adjustment. The difference between  $A$  and  $A_0$  is always kept below 1% during our simulation, so the cell area can

be regarded as constant. For sufficiently large  $P_0$ , the resulting  $P$  is independent of the value of  $P_0$ .

3) After the corridor formation, the pressure on each lobe is assumed to depend on the area of the lobe:  $P' = P'_0 (A_p / A_0)$ , where  $P'_0$  is a constant and  $A_p$  is the area of the lobe.

The pressure force on node  $i$  in the lobe is  $f'_p(i) = P'(r_{i,i-1} + r_{i,i+1}) / 2$ .

The bundling effect in the corridor is treated as dynamic springs connecting node pairs on the two opposite sides of the cell. A bundling spring is created when two nodes on the opposite sides are closer than the width of the corridor plus the segment length of the microtubule-bundle. We assume that the rest length of each newly created bundling spring,  $l_0$ , is equal to the distance between the two connected nodes. To produce the ‘zipping’ effect, we further assume that  $l_0$  decreases at a constant rate to bring the MT bundles together. The contraction force exerted from a bundling spring on the connected nodes is  $f_{\text{bundle}} = k_{\text{bundle}} (l - l_0)$ , where  $k_{\text{bundle}}$  is the spring constant of the bundling springs and  $l$  is the actual distance between the two connected nodes.

If the stretching force in a bundling spring is greater than a critical value, the bundling spring is removed to represent the bond detachment. This detachment force can be obtained from the binding energy per unit length  $\rho$  along the MT bundle. Let  $\xi$  be the segment length of nodes along the MT bundle. Each detachment event will release a binding energy  $\rho\xi$ , which should be equal to the elastic energy stored in the bundling spring before detachment. Therefore, the detachment force is  $f_{\text{detach}} = \sqrt{2k_{\text{bundle}}\rho\xi}$ .

To mimic the observed width of the corridor, the corridor in our simulation is further defined to have a minimum width of 0.2  $\mu\text{m}$  by imposing a hard-core interaction force between nodes on the opposite sides. Once the MT bundle becomes part of the narrow corridor, we assume that the bundling springs in that region stop shrinking such that the MT bundle is stabilized.

With all these forces, each node is moved according to the force balance:

$$\Delta\vec{r} = \begin{cases} (\vec{f}_s + \vec{f}_b + \vec{f}_p) / 2k_s & \text{before corridor formation,} \\ (\vec{f}_s + \vec{f}_b + \vec{f}'_p) / 2k_s + \vec{f}_{\text{bundle}} / k_{\text{bundle}} & \text{after corridor formation,} \end{cases}$$

where factor 2 in front of  $k_s$  is due to the fact that each node connects to two springs.

Here we assume that a pressure force exists to keep the cell area constant before the corridor formation. After the corridor formation, pressure from the cortex contraction as well as the the bundling proteins start to ‘zip up’ the corridor. In our simulation, every time there is a small change in the total microtubule-bundle length,  $10^4$  such relaxation steps are followed for the loop to reach equilibrium. After the relaxation, the bending

energy is obtained as  $E_b = (k_b / 2) \sum_{i=1}^N (\Delta\theta_i)^2$ . The force at node  $i$  is the spring force  $f_s(i)$

and the average force is  $\langle f_s \rangle = (1 / N) \sum_{i=1}^N f_s(i)$ .

### Choice of parameters

The flexural rigidity of a bundle of 7 MTs is roughly  $YI = 7l_p k_B T \approx 28 \text{ pN} \cdot \mu\text{m}^2$  if the MTs in the bundle can slide freely against each other. Here,  $l_p \approx 1 \text{ mm}$  is the persistence length of a single microtubule<sup>1-4</sup>. For a circular loop of radius  $R$  with  $N$  nodes being

evenly distributed along its perimeter, the bending spring constant  $k_b$  for each node can be estimated as follows: the bending energy of a circular loop is given by  $E = (YI / 2) \int (1 / R^2) ds = \pi YI / R$ . This energy can also be expressed as the sum of the bending energy from all  $N$  nodes  $E = (k_b / 2) \sum_N (\Delta\theta)^2 = 2\pi^2 k_b / N$ , where  $\Delta\theta = 2\pi / N$  is the bending angle at each node. Equating these two equations yields  $k_b = YI / \xi$ , where  $\xi = 2\pi R / N$  is the length of each spring. The stretching spring constant for each spring is estimated to be  $k_s \approx k_b / \xi^2$ , meaning that the energy for bending the two adjacent springs by  $60^\circ$  is similar to that for stretching a spring by  $\xi$ . For a circle with a perimeter of  $10 \mu\text{m}$  and  $N = 80$ , we have  $k_b \approx 220 \text{ pN}\cdot\mu\text{m}$  and  $k_s \approx 1.4 \times 10^4 \text{ pN}/\mu\text{m}$ . As the MT bundle elongates,  $\xi$  increases, thus both  $k_s$  and  $k_b$  decrease. We estimate that  $k_{\text{bundle}}$  has the same order of magnitude as  $k_s$ , since  $k_{\text{bundle}}$  is not affected by the elongation of the MT bundle, we take  $k_{\text{bundle}} = YI / (L_0 / N)^3$ . The value of  $\rho$  for the bundling proteins is manually chosen to be about  $2.5 \text{ pN}$  such that the simulated PLT diameter matches the observed value of about  $\sim 2 \mu\text{m}$ .

We choose  $P_0 = k_s$  and  $P'_0 = 4 \text{ pN}/\mu\text{m}$  to match the observed lobe size for filamin-KO PLTs.

### Analytical Model

Let  $x(s)$  and  $y(s)$  describe the path traced out by the microtubule peripheral bundle in the platelet where  $s$  is the arc-length parameter. Let  $\psi(s)$  denote the angle made by the tangent vector and the  $x$ -axis. The energy of the bundle can be written as:

$$E = \int YI (\psi')^2 + \lambda_A (xy' - yx') + \lambda_y (s) (y' - \sin(\psi)) + \lambda_x (s) (x' - \cos(\psi)) ds$$

$\lambda_A$  is the Lagrange multiplier for the surface area constraint. The final two terms are non-holonomic constraints (with Lagrange multipliers  $\lambda_y(s)$  and  $\lambda_x(s)$ ) ascertaining that  $x' = \cos(\psi)$  and  $y' = \sin(\psi)$  which enforces the microtubule non-extensibility constraint that fixes the total length of the microtubule peripheral bundle.

The corresponding Euler-Lagrange equations that minimize energy  $E$  are:

$$2YI\psi'' + \lambda_y \cos(\psi) + \lambda_x \sin(\psi) = 0$$

$$-2\lambda_A y' + \lambda_x' = 0$$

$$\lambda_A x' + \lambda_y' = 0$$

$$x' - \cos(\psi) = 0$$

$$y' - \sin(\psi) = 0$$

We shall assume periodic boundary condition so that  $x(0) = x(L)$ ,  $y(0) = y(L)$ , and  $\psi(0) = \psi(L)$  where  $L$  is the total contour length of the platelet cell. The second and third equations can be integrated directly and plugged into the first equation to further integrate and simplify the first equation to the following form:

$$2YI\psi' = -\lambda_A (x^2 + y^2) + c_1 x + c_2 y + c_3$$

where  $c_1, c_2, c_3$  are integrating constants. We non-dimensionalize these equations by dividing the first equation by  $2YI$  and setting  $\kappa = -\lambda_A/(2YI)$ . By shifting our coordinate system, the first equation can be written simply as:

$$\psi' = \kappa \rho^2 - c_0$$

where  $\rho^2 = x^2 + y^2$ . Taking the derivative of the final two equations and plugging in  $\psi'$ , we get

$$x'' = -(\kappa\rho^2 - c_0)y'$$

$$y'' = (\kappa\rho^2 - c_0)x'$$

This is the simplest form of the equations we need to solve. The goal is to find a closed path solution and choose parameters  $\kappa$  and  $c_0$  to satisfy the fixed area and fixed length constraints. The advantage of this form is that the non-holonomic constraints are removed.

Numerically solving the above equations is still daunting. We can simplify the calculation considerably by noting that the above equations can be derived from minimizing the following functional integral:

$$H = \int \left[ (x'^2 + y'^2) / 2 + x'B_x(x, y) + y'B_y(x, y) \right] ds$$

where the only condition on  $B_x, B_y$  is:

$$\frac{dB_y}{dx} - \frac{dB_x}{dy} = -(\kappa\rho^2 - c_0)$$

Since  $x'^2 + y'^2 = \cos(\psi)^2 + \sin(\psi)^2 = 1$ , the first part of the integral may be written as simply  $L/2$ . Using Green's theorem, the rest of the expression may be written as an integral over the area ( $A$ ) enclosed by the closed path, the solution that we seek. The final expression is

$$H = L/2 - \int (\kappa\rho^2 - c_0) dA$$

This expression offers an easy way to numerically approximate the solution using trial function method. The idea is to use a trial function parameterized by a handful of

variational parameters and express  $H$  in terms of these parameters followed by minimization with respect to the parameters. Given the expected final shape, we use the trial function of the following form:

$$x(t) = \alpha \cosh(\beta + \gamma \cos(2t)) \cos(t)$$

$$y(t) = \alpha \sinh(\beta + \gamma \cos(2t)) \sin(t)$$

where  $\alpha$ ,  $\beta$  and  $\gamma$  are the variational parameters. It is important to note that  $t$  is not the arc-length variable  $s$  so care needs to be taken when performing the integration, namely  $ds = \sqrt{(dx/dt)^2 + (dy/dt)^2} dt$ . We used software *Mathematica*<sup>TM</sup> to determine the optimal parameters that minimize integral  $H$  and simultaneously fix area ( $A$ ) and length ( $L$ ). Once the optimal parameters that minimize  $H$  are determined, we can use the resulting functions  $x(t)$  and  $y(t)$  to plot the shape and calculate the curvature energy (see Fig. S6c).

## Results

1. Figure 6b shows the simulated shapes of a proPLT with different contour lengths in the case when zipping effect, not the external pressure, determines the shape after the corridor is formed. The corridor has a minimum width of 0.2  $\mu\text{m}$ . If the external pressure keeps the cell area constant during the elongation, the cell will deform into a barbell shape due to the compression of the external pressure and the bending of the MT bundle (Fig. 6a, Supplementary Fig. 6a online). This shape transition has also been confirmed by our analytical calculation above. With the constant area assumption, the area of the final PLTs decreases linearly with the contour length because the area in the corridor region increases linearly with the contour length but the shape of the two lobes on the two ends

of the proPLT remains the same. As a result, the area of the corridor increases with the contour length and the area of the two lobes decreases.

After the formation of the corridor, both the cortex pressure and the ‘zipping’ effect lead to the separation of the two lobes (Fig. 6a). The ‘zipping’ effect will keep extending the corridor and shrinking the two lobes until the effective binding force is balanced by the force in the MT bundle. The size of the final PLT thus depends on the detachment force of the bonds and is independent of the length of the corridor. The observed mean diameter of final PLTs is  $D = 2.3 \mu\text{m}$ . Our simulation shows that a binding energy density of  $\rho \approx 2.5 \text{ pN}$  and a pressure coefficient of  $P'_0 = 4 \text{ pN}/\mu\text{m}$  are required to obtain final PLTs of this size.

2. Dependence of the extension ratio on the initial size reveals a critical cell size: The data that we obtained directly from microscopy is a collection of proPLTs’ contour length  $L$  and the corresponding area  $A$ . If a proPLT is initially circular and its area is unchanged during the extension, we can estimate its initial contour length to be  $L_0 = \sqrt{4\pi A}$ . We then show all the collected data on a  $L/L_0 - L_0$  plot (Fig. 6c). We find a critical cell perimeter of  $10 \mu\text{m}$ . Cells with  $L_0 < 10 \mu\text{m}$  stay circular ( $L/L_0 = 1$ ), while cells with  $L_0 > 10 \mu\text{m}$  have elongated shape ( $L/L_0 > 1$ ). Further investigation shows that the extension ratio for cells with  $L_0 > 10 \mu\text{m}$  follows  $L/L_0 \approx L_0/10 \mu\text{m}$ , or  $L \approx L_0^2 / (10 \mu\text{m})$ . There are two possible mechanisms determining the critical size: a) a force barrier for MT-sliding motors; b) available tubulin scales with cell area; c) area conservation.

- a) To deform a proPLT, motors that extend the MT bundle have to generate enough sliding force along the microtubule-bundle to overcome the resisting force. Our simulation shows that force in the MT bundle decreases with  $L/L_0$  (Supplementary Fig. 6b-d online). The maximum force barrier is at  $L/L_0=1$ . This force barrier has also been calculated previously <sup>5</sup>: for a circular loop with  $L_0 = 2\pi R$ , the force barrier is  $F \approx (YI/2)(1/R^2 + 5/R^2) \approx 120YI/L_0^2$ , where the term  $1/R^2$  is from the bending and the term  $5/R^2$  is from the constraint for the two-lobed bending mode. This is consistent with our simulation result that  $F$  is between  $100YI/L_0^2$  and  $150YI/L_0^2$  (Supplementary Fig. 6d online). For  $L_0 = 10 \mu\text{m}$ , this maximum force barrier is about 40 pN, indicating that the maximum available sliding force from the motors is about 40 pN. If this maximum motor force is the same for all cells, cells with  $L_0 < 10 \mu\text{m}$  will not be able to deform from the initial circular shape since the maximum force barrier is inversely proportional to  $L_0^2$ .
- b) If the amount of available tubulin is proportional to  $A$ , the final length of the microtubule-bundle is  $L \propto A \propto L_0^2$ . This explains the distribution of  $L \approx L_0^2 / (10 \mu\text{m})$  for  $L_0 > 10 \mu\text{m}$ . For  $L_0 < 10 \mu\text{m}$ , this formula predicts that there is not enough MT overlap to maintain necessary tension.
- c) Because the lobes typically have a fixed characteristic area  $A_c$ , the cell area is  $A = 2A_c + w \cdot d$ , where  $w$  is the corridor width and  $d$  is its length. If  $w$  is a constant and  $L_c \approx \sqrt{4\pi A_c}$  is the contour length of each lobe, the contour length of

the cell is  $L = 2(L_c + d) \approx 2(L_c + (A - 2A_c)/w)$ , which depends linearly on  $A$ , and therefore  $L \propto L_0^2$  for  $L_0 > 10\mu m$ .

3. Size of final PLT depends on the number of MTs in the bundle: In our simulation, we assume that  $YI$  is proportional to the number of microtubules in the bundle. The force in the neck region of the lobe can be estimated as  $F \propto dE/dR \propto YI/D^2 \propto N/D^2$ . If this force is equal to the constant detachment force for the bundling proteins, we have  $D \propto N^{1/2}$ .

4. Effect of pressure on the size of the final PLT: In the above simulation, we ignored forces from cortex contraction after the formation of corridor. To quantitatively understand how the external pressure affects the size of the final PLT, we impose a constant pressure  $P$  to the proPLT after the formation of the corridor. Our simulation shows a power law relation  $D \propto P^{-1/4}$  (Supplementary Fig. 6e online). This can be roughly explained as follows. Since the bending energy of a circular microtubule-bundle scales as  $E \propto YI/R$ , the radial force exerted scales as  $F_n = dE/dR \propto YI/R^2$ . Therefore, the pressure required to balance this force is  $P = F_n/2\pi R \propto YI/R^3$ , which gives  $D = 2R \propto P^{-1/3}$ .

5. Effect of twisting of the MT-bundle

If MTs in the corridor's bundle are twisted into a helical form, the coordinates of a MT can be expressed with the following parametric equation:

$$x = r \cos(2\pi t), \quad y = r \sin(2\pi t), \quad z = \lambda t,$$

where  $r$  is the radius of the helix,  $\lambda$  is the pitch of the helix and  $t$  is a parameter. Assuming that  $r \ll \lambda$ , the curvature of the helix is a constant:

$$\kappa = \frac{r}{r^2 + (\lambda / 2\pi)^2}.$$

The total bending energy for the helix of two MTs is:

$$E_1 = YI \int \kappa^2 ds = YI L \left[ \frac{r}{r^2 + (\lambda / 2\pi)^2} \right]^2,$$

where  $L$  is the MT contour length. If the density of the bundling energy is a constant,  $J$ , the bundling energy of these two MTs is

$$E_2 = -JL.$$

The total energy in the helix is the sum of the above two energies:

$$E = E_1 + E_2 \approx YI L \left[ \frac{r}{r^2 + (\lambda / 2\pi)^2} \right]^2 - JL.$$

If the corridor length  $z$  is fixed, then we

have:  $L = \sqrt{z^2 + (2\pi nr)^2} = z\sqrt{1 + 4\pi^2 r^2 / \lambda^2}$ , where  $n = z / \lambda$  is the number of turns of each

MT. Plugging  $L$  into the expression for  $E$ , the value of  $\lambda$  satisfying  $dE / d\lambda = 0$  can be solved numerically. We plot the total energy as a function of the helical pitch in Supplementary Fig. 6f online. From the plot, it is obvious that the equilibrium configuration corresponds to the twisted bundle.

## References

1. F. Gittes, B. Mickey, J. Nettleton et al., *J Cell Biol* **120** (4), 923 (1993).
2. M. E. Janson and M. Dogterom, *Biophys J* **87** (4), 2723 (2004).
3. F. Pampaloni, G. Lattanzi, A. Jonas et al., *Proc Natl Acad Sci U S A* **103** (27), 10248 (2006).
4. M. G. Van den Heuvel, M. P. de Graaff, and C. Dekker, *Proc Natl Acad Sci U S A* **105** (23), 7941 (2008).
5. G. Arreaga, R. Capovilla, C. Chryssomalakos et al., *Phys Rev E Stat Nonlin Soft Matter Phys* **65** (3 Pt 1), 031801 (2002).